

## A Tale of Two Origins: In-Situ versus Accreted Nitrogen-Rich Field Stars in the MW

YI QIAO,<sup>1,2</sup> BAITIAN TANG,<sup>1,2</sup> JOSÉ G. FERNÁNDEZ-TRINCADO,<sup>3,4</sup> MINGJIE JIAN,<sup>5</sup> CARLOS ALLENDE PRIETO,<sup>6,7</sup>  
HONGLIANG YAN,<sup>8</sup> ZHEN YUAN,<sup>9,10</sup> YANG HUANG,<sup>8</sup> THOMAS MASSERON,<sup>6,7</sup> BEATRIZ BARBUY,<sup>11</sup> JIANRONG SHI,<sup>8</sup>  
CHENGYUAN LI,<sup>12,2</sup> RUOYUN HUANG,<sup>12,2</sup> JIAJUN ZHANG,<sup>12,2</sup> JING LI,<sup>13</sup> CHAO LIU,<sup>14,15</sup> AND WEISHAN ZHU<sup>12,2</sup>

<sup>1</sup>*School of Physics and Astronomy, Sun Yat-sen University, Daxue Road, Zhuhai, 519082, P.R.China; tangbt@mail.sysu.edu.cn*

<sup>2</sup>*CSST Science Center for the Guangdong-Hong Kong-Macau Greater Bay Area, Zhuhai, 519082, P.R.China*

<sup>3</sup>*Universidad Católica del Norte, Núcleo UCN en Arqueología Galáctica - Inst. de Astronomía, Av. Angamos 0610, Antofagasta, Chile*

<sup>4</sup>*Universidad Católica del Norte, Departamento de Ingeniería de Sistemas y Computación, Av. Angamos 0610, Antofagasta, Chile*

<sup>5</sup>*Department of Astronomy, AlbaNova University Center, Stockholm University, SE-106 91 Stockholm, Sweden*

<sup>6</sup>*Instituto de Astrofísica de Canarias, C/Vía Lactea s/n, 38205 La Laguna, Tenerife, Spain*

<sup>7</sup>*Departamento de Astrofísica, Universidad de La Laguna, 38206 La Laguna, Tenerife, Spain*

<sup>8</sup>*CAS Key Laboratory of Optical Astronomy, National Astronomical Observatories, Chinese Academy of Sciences, Beijing 100012, P.R.China*

<sup>9</sup>*School of Astronomy and Space Science, Nanjing University, Key Laboratory of Modern Astronomy and Astrophysics (Nanjing University), Ministry of Education, Nanjing 210093, P.R.China*

<sup>10</sup>*Key Laboratory of Modern Astronomy and Astrophysics, Nanjing University, Ministry of Education, Nanjing 210093, China*

<sup>11</sup>*Universidade de São Paulo, IAG, Departamento de Astronomia, 05508-090 São Paulo, Brazil*

<sup>12</sup>*School of Physics and Astronomy, Sun Yat-sen University, Daxue Road, Zhuhai, 519082, P.R.China*

<sup>13</sup>*School of Physics and Astronomy, China West Normal University, 1 ShiDa Road, Nanchong, 637002, P.R.China*

<sup>14</sup>*Key Laboratory of Space Astronomy and Technology, National Astronomical Observatories, Chinese Academy of Sciences, Beijing 100101, P.R.China*

<sup>15</sup>*Institute for Frontiers in Astronomy and Astrophysics, Beijing Normal University, Beijing 102206, P.R.China*

(Received XXX)

Submitted to The Astrophysical Journal

### ABSTRACT

Spectroscopic surveys have identified significant numbers of metal-poor nitrogen-rich (N-rich) field stars. These stars are strong candidates for escapees from globular clusters (GCs), as their distinctive nitrogen enhancement mirrors the chemical patterns observed in some of the members of GCs. As part of the effort to characterize their chemodynamical properties, we derived abundances for up to 25 elements in a sample of 33 N-rich field giant stars (18 of them are studied for the first time) using high-resolution optical spectroscopy. We confirm their elevated abundances of N, Na, and Al, strongly supporting a GC origin. Given that Galactic GCs themselves formed within diverse progenitor galaxies, we sought to identify the ancestral systems of these N-rich field stars. By analyzing their dynamical parameters, we separated the sample into high-energy (HE) and low-energy (LE) groups. The HE group exhibits lower  $[\alpha/\text{Fe}]$  and enhanced  $r$ -process abundances compared to the LE group. This indicates that the HE stars likely escaped from GCs accreted from massive dwarf galaxies (e.g., Gaia-Sausage-Enceladus), while the LE stars probably originated from in-situ GCs. We also find that the chemical pattern of these N-rich stars with  $[\text{Fe}/\text{H}] \lesssim -1.0$  are similar to the high-redshift “N-emitters”. Furthermore, orbital integrations revealed a close encounter between one N-rich field star and the globular cluster NGC 6235. Our work demonstrates the potential of using chemodynamical analyses to trace Galactic assembly through chemical peculiar stars, while highlighting that larger samples and more precise data in the future are crucial to establish definitive origins.

**Keywords:** Globular star clusters(564) — Chemical abundances(224) — Milky Way Halo(1050) — Nitrogen enhanced stars(20) — Stellar dynamics(1596) — Stellar kinematics(1608)

### 1. INTRODUCTION

The Milky Way (MW) represents a archetypal laboratory for studying galaxy formation through hierarchi-

cal assembly. Seminal studies established that the MW halo preserves fossil records of accretion events, where tidally disrupted dwarf galaxies (Sagittarius) imprint kinematical and chemical substructures (Ibata et al. 1994; Majewski et al. 2003; Sbordone et al. 2007; Haselquist et al. 2021). This paradigm was revolutionized by Gaia astrometry and panoramic spectroscopic surveys (e.g., Sloan Digital Sky Survey — SDSS, Blanton et al. 2017; LAMOST Galactic spectroscopic survey, Cui et al. 2012; Deng et al. 2012; Zhao et al. 2012). The newly identified Gaia-Sausage-Enceladus (GSE) merger is an accretion event that contributed a substantial amount of mass to the inner halo (Belokurov et al. 2018; Helmi et al. 2018; Myeong et al. 2018, 2019), while the MW’s stellar disk shows dynamical signatures of disequilibrium, such as phase spirals (Antoja et al. 2018), spiral arms, and ripples (Laporte et al. 2020; Qiao et al. 2024). Earlier studies (Carollo et al. 2010; Nissen & Schuster 2010; Beers et al. 2012) had already identified the halo’s dual structures, inner (high- $[\alpha/\text{Fe}]$ ) and outer (low- $[\alpha/\text{Fe}]$ ) components, reflecting distinct accretion histories. Globular clusters (GCs) serve as critical tracers since they share the dynamical and chemical signatures of their host accretion systems (Massari et al. 2019; Lin et al. 2025), bridging galactic and cluster-scale evolution.

The discovery of multiple populations (MPs) in GCs significantly altered our understanding of star formation environments. Carretta et al. (2009a,b) demonstrated that light elements’ variations (e.g., Na-O anticorrelations) are ubiquitous in GCs. It is suggested such variations arise from high temperature ( $T > 7 \times 10^7$  K) proton-capture nucleosynthesis, possibly occurring in early generations of massive stars, such as fast-rotating massive stars (FRMS), supermassive stars, or AGB stars (D’Ercole et al. 2011; Carretta et al. 2011; Bastian & Lardo 2018). MPs may originate from self-enrichment by these stars, polluting the intracluster medium with processed material. A more metal-poor, and compact environment is preferred for the formation of MPs in GCs (Krause et al. 2016; Huang et al. 2024). Dynamical modeling indicates that tidal interactions with the MW stripped more than 50 percent of GC stars into the halo over cosmic time (Baumgardt & Makino 2003), and escaped stars should retain MPs signatures, including N, Na, and Al enrichment, enabling their identification as relics of dissolved clusters (Lind et al. 2015; Martell et al. 2016; Schiavon et al. 2017).

Among the aforementioned enriched elements in GCs, N is easier to estimate through molecular bands (e.g., CN bands around 3883 and 4215 Å). Therefore, N-rich field stars have emerged as powerful trac-

ers of GC tidal disruption and accretion events within the MW. Low-resolution surveys (SDSS/SEGUE, LAMOST) firstly identified such stars through CN-band enhancements, associating them with escaped GC second generations (Martell et al. 2011; Tang et al. 2019; Yan et al. 2022). APOGEE spectroscopy later confirmed their distinct chemistry: anomalous  $[\text{C}/\text{N}]$ ,  $[\text{Al}/\text{Fe}]$ , and  $[\text{Mg}/\text{Fe}]$  ratios mirroring features of GC enhanced populations, indicative of proton-capture processes in dense cluster environments (Schiavon et al. 2017; Fernández-Trincado et al. 2017, 2019, 2022). Detailed studies further revealed kinematic subgroups: while most align with in-situ halo dynamics, 15–30 percent exhibit high-eccentricity “sausage-like” orbits characteristic of GES-like mergers (Tang et al. 2020; Kisku et al. 2021; Yu et al. 2021). Kinematic data and dynamical modeling also enabled their associations with specific GCs (Savino & Posti 2019; Xu et al. 2024).

Despite progress mentioned above, more comprehensive and detailed chemodynamical patterns of N-rich stars, as well as more robust connections with GCs, are still lacking. Similar dynamics (e.g., overlaps in Toomre diagrams) alone cannot distinguish escape events from co-natal stars in accreted systems. Meanwhile, limited observational constraints of heavier elements hinder origin discrimination and r/s-process diagnostics of host environments. These gaps impede a unified understanding of how cluster dissolution and hierarchical assembly collectively shape the N-rich field star populations.

An important preceding work, Yu et al. (2021), confirmed that the chemical abundances (e.g., Na, Al,  $\alpha$  elements) of 15 N-rich field stars are similar to GC stars using high-resolution spectroscopy and identified one star with chemical signatures indicative of a GSE origin. Our work significantly expands the previous one by analyzing a larger sample of 33 N-rich field stars (including the 15 stars mentioned above) with high-resolution optical spectra (Section 2) to study more species and conducting a systematic orbital analysis. We classify the N-rich stars into High-Energy (likely accreted) and Low-Energy (likely in-situ) groups, revealing clearer chemical distinctions between them (such as r/s-process ratios), thereby more precisely tracing their origins (Section 3). Furthermore, in Section 4, we link metal-poor N-rich field stars to high-redshift “N-emitters” and, through orbital integration, provide evidence for an N-rich star possibly ejected from the globular cluster NGC 6235, marking methodological and scientific progress. A brief summary is given in Section 5.

## 2. DATA AND METHODS

**Table 1.** Stellar Parameters and Chemical Abundances for 8 N-rich Field Stars Observed with CFHT.

| Object                           | Num28   | Num32    | Num24    | Num7     | Num63    | Num1     | Num37    | Num10    |
|----------------------------------|---------|----------|----------|----------|----------|----------|----------|----------|
| RA (J2000)                       | 13.1551 | 140.2051 | 115.7504 | 145.2212 | 239.9169 | 260.9612 | 180.2667 | 286.7982 |
| Dec (J2000)                      | 37.6988 | 32.4165  | 15.5836  | 25.7415  | 32.446   | 49.5797  | -0.9752  | 39.1366  |
| $T_{\text{eff}}$ (K)             | 4775    | 5065     | 5271     | 4283     | 4558     | 4707     | 4920     | 4458     |
| $\log g$                         | 1.57    | 2.56     | 1.95     | 1.05     | 1.16     | 1.70     | 2.25     | 1.33     |
| [Fe/H]                           | -1.060  | -1.245   | -1.260   | -1.125   | -1.790   | -1.370   | -1.390   | -1.110   |
| $V_{\text{mic}}$ (km s $^{-1}$ ) | 1.74    | 1.32     | 1.71     | 2.00     | 1.80     | 1.75     | 1.57     | 2.12     |
| RV (km s $^{-1}$ )               | 3.93    | -1.44    | -139.73  | 207.00   | -141.95  | -207.05  | 134.62   | -312.34  |
| [O/Fe]                           | 0.57    | 0.58     | 0.48     | 0.54     | 0.06     | 0.31     | 0.52     | 0.56     |
| [Mg/Fe]                          | 0.64    | 0.37     | 0.55     | 0.30     | 0.47     | 0.59     | 0.50     | 0.55     |
| [Si/Fe]                          | 0.34    | 0.28     | 0.50     | 0.20     | 0.39     | 0.33     | 0.38     | 0.23     |
| [Ca/Fe]                          | 0.37    | 0.31     | 0.30     | 0.19     | 0.45     | 0.40     | 0.46     | 0.36     |
| [Ti/Fe]                          | 0.44    | 0.24     | 0.27     | 0.36     | 0.28     | 0.35     | 0.33     | 0.50     |
| [Na/Fe]                          | 0.72    | 0.11     | -0.06    | -0.02    | 0.50     | 0.02     | -0.041   | 0.36     |
| [Al/Fe]                          | 0.53    | 0.28     | 0.64     | 0.26     | 1.12     | 0.33     | 0.32     | 0.28     |
| [Sc/Fe]                          | 0.28    | 0.06     | 0.14     | 0.25     | 0.03     | 0.21     | 0.28     | 0.08     |
| [Cr/Fe]                          | 0.04    | -0.09    | -0.07    | -0.02    | 0.02     | 0.04     | 0.00     | 0.12     |
| [Mn/Fe]                          | 0.10    | -0.27    | -0.34    | -0.28    | -0.27    | -0.14    | -0.32    | -0.13    |
| [Co/Fe]                          | 0.49    | 0.01     | -0.23    | -0.04    | -0.03    | -0.08    | -0.13    | -0.01    |
| [Ni/Fe]                          | 0.15    | -0.02    | 0.06     | -0.06    | -0.04    | 0.08     | 0.07     | 0.00     |
| [V/Fe]                           | 0.27    | 0.03     | 0.05     | 0.22     | 0.11     | 0.24     | 0.15     | 0.39     |
| [Ba/Fe]                          | 0.48    | 0.74     | 1.02     | 0.47     | -0.14    | -0.26    | 0.97     | 0.78     |
| [La/Fe]                          | 0.23    | 0.35     | 0.47     | 0.76     | 0.26     | 0.34     | 1.02     | 1.06     |
| [Ce/Fe]                          | 0.01    | 0.21     | 0.22     | 0.30     | 0.00     | 0.06     | 0.76     | 0.52     |
| [Eu/Fe]                          | 0.34    | 0.45     | 0.46     | 0.94     | -        | 0.71     | 0.62     | 1.14     |
| [Y/Fe]                           | -0.18   | 0.14     | 0.16     | -0.11    | -0.30    | -0.22    | 0.59     | 0.05     |
| [Nd/Fe]                          | 0.16    | 0.23     | 0.23     | 0.71     | 0.21     | 0.28     | 0.85     | 0.78     |
| [Zr/Fe]                          | 0.29    | 0.29     | 0.70     | 0.54     | 0.23     | 0.23     | 0.94     | -        |

High-resolution spectra were obtained for 23 N-rich field stars selected from Tang et al. (2019, 2020), in which the original selection from LAMOST was based on a direct comparison of spectral indices measuring the strength of molecular bands. N-rich candidates were identified by anomalously strong CN bands (at  $\sim 3883$  Å and  $\sim 4215$  Å) relative to a normal CH band (at  $\sim 4300$  Å) (Harbeck et al. 2003). This differential index approach effectively isolated stars with enhanced nitrogen without requiring absolute abundance measurements from the low-resolution spectra. About the 23 N-rich field stars: (1) 8 of them were observed with the ESPaDOnS (Echelle SpectroPolarimetric Device for the Observation of Stars, Donati et al. 2006) on the Canada-France-Hawaii Telescope (CFHT). This spectrograph offers high-resolution spectra with large wavelength coverage ( $R = 68000$ ,  $3700 < \lambda < 10500$  Å). These spectra were obtained between November 2020 and July 2023 as part of the Telescope Access Program. The signal-to-noise ratios (SNR) per pixel typically exceed 60 be-

tween 4300 - 8600 Å. (2) 15 of them were observed with the MIKE (Magellan Inamori Kyocera Echelle, Bernstein et al. 2003) on the Magellan Clay telescope. The MIKE spectra achieve nominal spectral resolution of 35000/28000 on the blue side ( $3200 < \lambda < 5000$  Å) and the red side ( $4900 < \lambda < 10000$  Å), respectively. Yu et al. (2021) have presented an analysis of 21 elemental abundances of these 15 stars. In addition, we derive the abundances of C, N, Cu, and Zn in this work.

To further enlarge the N-rich field star sample with optical high-resolution spectra, we crossmatched the APOGEE-selected N-rich field star sample (Fernández-Trincado et al. 2022) with the GALAH Data Release (DR) 4 (Buder et al. 2025). Note that the metallicity cut in the APOGEE N-rich field stars is  $[-1.8, -0.7]$ , which is different than that of LAMOST-selected stars ( $[-1.8, -1.0]$ ). The GALAH DR4 spectra, obtained using the HERMES spectrograph, cover four distinct wavelength bands (blue: 4675–4949 Å; green: 5624–5900 Å; red: 6424–6775 Å; and near-infrared: 7549–7925 Å) with a

**Table 2.** Chemical Abundances of C, N, Cu and Zn for 23 LAMOST-selected N-rich Field Stars.

| Object | [C/Fe] | [N/Fe] | [Cu/Fe] | [Zn/Fe] |
|--------|--------|--------|---------|---------|
| Num28  | 0.15   | 1.09   | 0.02    | 0.37    |
| Num32  | 0.12   | 1.00   | -0.33   | 0.24    |
| Num24  | 0.05   | 0.78   | -0.46   | 0.13    |
| Num7   | -0.41  | 0.78   | -0.95   | 0.00    |
| Num63  | -0.59  | 1.06   | -0.65   | 0.14    |
| Num1   | -0.34  | 0.84   | -0.70   | 0.03    |
| Num37  | -0.15  | 1.31   | -0.48   | 0.03    |
| Num10  | -0.19  | 0.73   | -0.40   | 0.27    |
| Num9   | -      | -      | -0.85   | -0.38   |
| Num38  | -0.61  | 1.59   | -0.47   | 0.27    |
| Num47  | -0.24  | 1.41   | -0.42   | 0.00    |
| Num58  | -0.21  | 1.66   | -0.49   | 0.07    |
| Num62  | -0.59  | 1.72   | -0.79   | 0.04    |
| Num65  | -      | -      | -0.27   | -0.09   |
| Num67  | -      | -      | -0.19   | 0.25    |
| Num69  | -      | -      | 0.25    | 0.22    |
| Num80  | -0.12  | 1.52   | -0.59   | 0.22    |
| Num82  | -0.14  | 0.84   | -0.33   | 0.27    |
| Num86  | -      | -      | -0.42   | -0.22   |
| Num88  | -      | -      | -0.55   | 0.15    |
| Num94  | 0.11   | 1.21   | -0.22   | 0.17    |
| Num97  | -      | -      | -0.27   | 0.34    |
| Num98  | -      | -      | -0.01   | 0.16    |

resolution of  $R \sim 28,000$ . 10 stars with high SNR (SNR  $> 50$  for blue and green bands, SNR  $> 75$  for red and NIR bands) were selected. In summary, we collected 33 (8 + 15 + 10) N-rich field stars (their observation information can be found in Table A2) with optical high-resolution spectra for subsequent analysis.

All ESPaDOnS spectra were reduced using standard pipelines, including bias correction, flat-fielding, cosmic ray removal, and wavelength calibration. Next, heliocentric radial velocities (RVs) were derived and corrected using iSpec (Blanco-Cuaresma et al. 2014). Our derived RVs are consistent with those published by Gaia DR3 within  $2 \text{ km s}^{-1}$ . We didn't find evidence of binaries after comparing RVs of different epochs ( $\Delta < 2 \text{ km s}^{-1}$ ).

The stellar atmospheric parameters and chemical abundances were derived using BACCHUS (Brussels Automated Code for Characterizing High accuracy Spectra) (Masseron et al. 2016), which is developed on top of the radiative transfer code Turbospectrum (Plez 2012). This procedure mainly follows Yu et al. (2021) for atomic chemical abundances and Tang et al. (2023)

for chemical abundances derived from molecular lines (e.g., C & N). We briefly recap the main steps here. The model atmospheres were interpolated from MARCS model grids (Gustafsson et al. 2008). The stellar parameters — effective temperature ( $T_{\text{eff}}$ ), surface gravity ( $\log g$ ), metallicity ( $[\text{Fe}/\text{H}]$ ) and microturbulence — were determined iteratively by enforcing excitation and ionization equilibrium for Fe I and Fe II lines. BACCHUS performs a line-by-line analysis, where observed spectra are compared with synthetic spectra of various abundances. The final abundance of a given element was derived by averaging the best-fit abundances from reliable multiple lines (BACCHUS gives abundance flags of each line and in this work we only chose the abundance values with flag = 0 or checked the lines by eye).

We determined the abundances of C & N in a self-consistent way. Besides atomic lines, multiple molecular lines are used here. C abundance is firstly derived from the CH lines, then N abundance is derived from the CN lines<sup>1</sup> (see Fig. A1 for sample spectra). The procedure is repeated until the derived abundances between two adjacent iterations converge ( $< 0.1$  dex). This process can minimize the dependence of the molecular lines. However, if the derived abundances do not converge after 50 iterations, they are not reported in this work. The non-convergence of C/N abundances for several stars is probably attributed to various reasons, such as locally lower S/N at specific wavelengths, limitations of the 1D atmospheric model grid, or intrinsic complexities in the spectra, rather than the absence of N-enhancement. Despite the non-convergence, these stars still exhibit strong CN bands and lines in their spectra. For the 10 stars in our GALAH/APOGEE sample, given that most C/N related spectral lines are absent or noisy in their optical GALAH spectra, we adopted the [C/Fe] and [N/Fe] derived by the APOGEE Stellar Parameter and Chemical Abundance Pipeline (ASPCAP, García Pérez et al. 2016) after checking their quality flags (ASPCAPFLAG = 0, C\_FE\_FLAG = 0, N\_FE\_FLAG = 0).

In summary, we determined abundances for 24 species, including light elements (C, N, O), odd-Z elements (Na, Al),  $\alpha$ -elements (Mg, Si, Ca, Ti), iron-peak elements (Sc, V, Cr, Mn, Co, Ni), neutron-capture elements (Y, Zr, Ba, La, Ce, Nd, Eu) and Cu, Zn. This approach ensures high-precision results suitable for studying the chemical evolution of N-rich field stars. The derived chemical abundances are given in Table 1, 2 & A1.

<sup>1</sup> These are not the same feature lines that we used to select N-rich field stars from LAMOST.

## 3. RESULTS

## 3.1. Chemical abundances

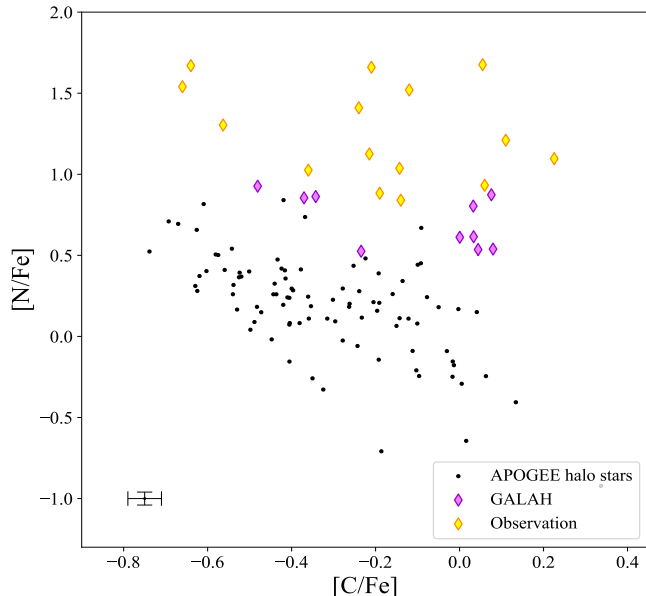


**Figure 1.** The  $[N/Fe]$  versus  $[C/Fe]$  plane. Yellow diamonds denote our observed N-rich field stars, while violet diamonds represent 10 GALAH/APOGEE N-rich field stars. The black dots indicate metal-poor RGB halo stars with similar stellar parameters as these N-rich field stars, and they are selected from the APOGEE survey. Typical abundance errors are shown in the corners of abundance panels.

**C & N:** Since the identification of N-rich field stars from LAMOST low-resolution spectra ( $R \sim 2000$ ) using CN and CH molecular bands, there have been concerns about its N-rich nature (Tang et al. 2019). Fig.1 clearly shows that the LAMOST-identified N-rich field stars (yellow diamonds) are strongly enhanced in nitrogen ( $[N/Fe] > 0.7$  dex). This level of N enhancement is clearly higher than those experienced by normal metal-poor RGB halo stars going through the first dredge-up and internal-mixing (black dots), where obvious C-N anti-correlation is found in the latter sample. Therefore, our LAMOST-identified N-rich field stars cannot be explained by these stellar evolution effects. The  $[N/Fe]$  ratios of 10 GALAH/APOGEE N-rich field stars (violet diamonds) are generally lower than those of the LAMOST-identified stars. This is caused by two factors: (1) The  $[N/Fe]$  limit between N-rich field stars and normal field stars drawn by Fernández-Trincado et al. (2022) decreases as the metallicity increases. This limit generally reflects the N enhancement by internal-mixing, which is a function of metallicity (Lagarde et al. 2012; Shetrone et al. 2019); (2) the GALAH/APOGEE N-rich field stars in this work are more metal-rich, where

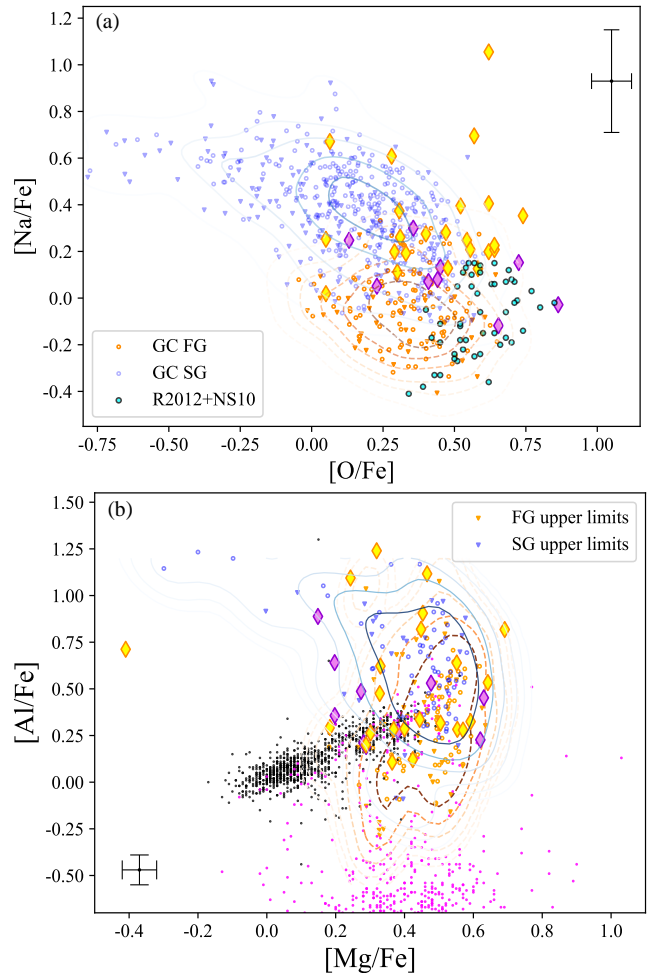


**Figure 2.** Panel a: The  $[Na/Fe]$  -  $[O/Fe]$  plane. Panel b: The  $[Mg/Fe]$  -  $[Al/Fe]$  plane. Markers of N-rich field stars are same as Fig.1. The Na and O abundances of individual stars in the GCs from Carretta et al. (2009b) are over-plotted for comparison. Orange and blue symbols correspond to GC first generation (FG) and second generation (SG) stars respectively. Upper limits in O and Al abundances are shown as triangles, while detections are shown as dots. The solid and dashed contours indicate the number densities of FG and SG, respectively. The field stars from Ramírez et al. (2012) and Nissen & Schuster (2010) shown as small cyan circles. The magenta dots correspond to MW halo stars (Fulbright 2000; Cayrel et al. 2004; Barklem et al. 2005; Yong et al. 2013; Roederer et al. 2014) and black dots are disk stars (Reddy et al. 2003, 2006; Bensby et al. 2014).

half of them show  $[Fe/H] > -0.9$  dex. Note that we did not apply the same metallicity cut as the LAMOST-identified stars, because we also want to check the properties of N-rich field stars in higher metallicity region.

**O & Na:** GC stars exhibit clear Na-O anti-correlation (background dots in Fig.2a), indicating the activation of high-temperature proton-capture chains (i.e., ON cycles and NeNa cycles, Arnould et al. 1999). Most of the

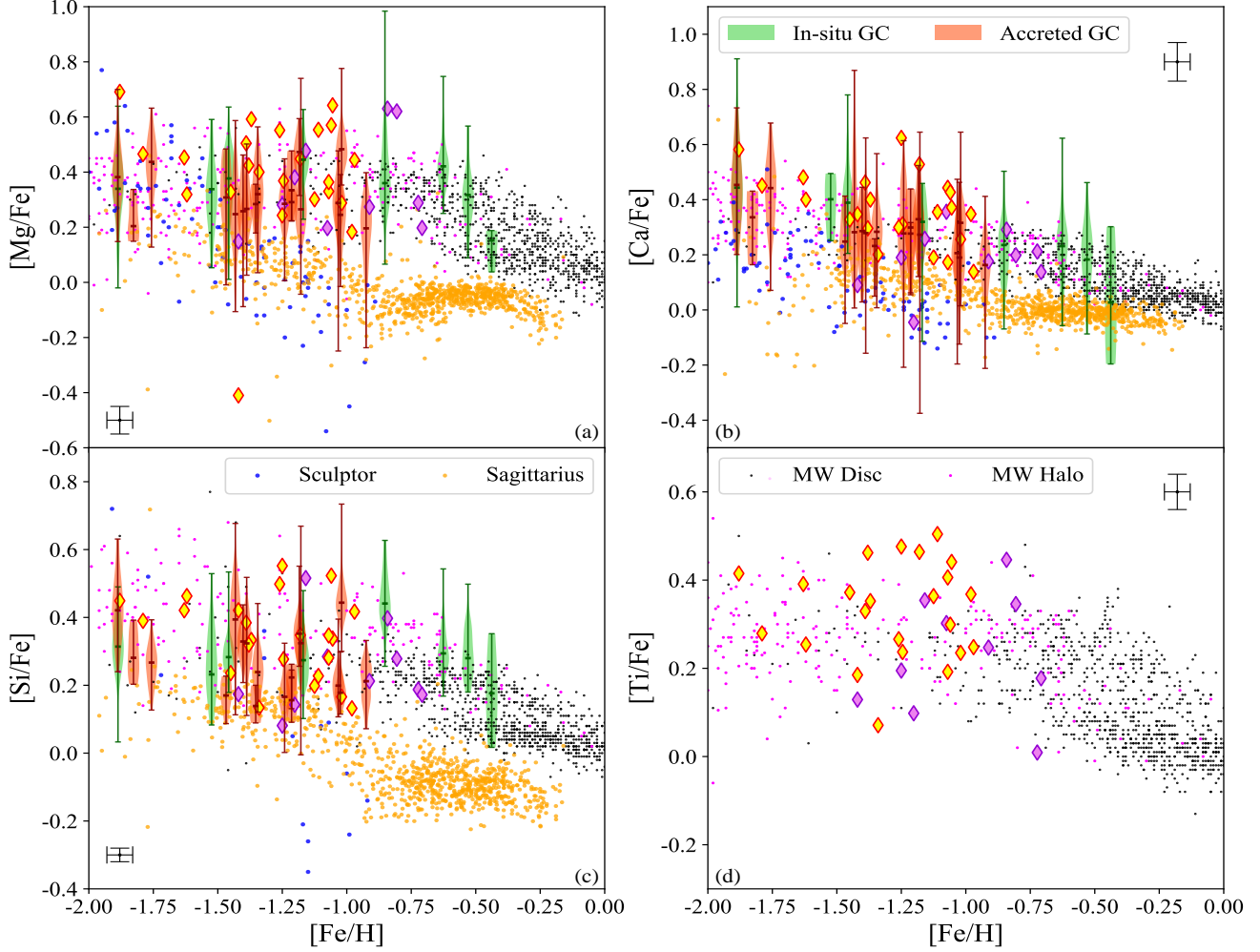


**Figure 3.** The  $[\alpha/\text{Fe}] - [\text{Fe}/\text{H}]$  planes, where  $\alpha$  elements include Mg, Si, Ca, and Ti. Violin shaped symbols indicate GC stars from APOGEE (Mészáros et al. 2020), including the average  $[\text{Fe}/\text{H}]$ , maximum and minimum  $[\alpha/\text{Fe}]$  of each GC. In-situ GCs are colored light green, while accreted GCs are light red. Orange circles correspond to Sagittarius (Hasselquist et al. 2017; Hayes et al. 2020). Blue circles represent stars from Sculptor (Hill et al. 2019). Other symbols are the same as Fig.2.

second-generation (SG) stars show  $[\text{Na}/\text{Fe}] > 0.15$ . In this context, the fact that most N-rich field stars also show  $[\text{Na}/\text{Fe}] > 0.15$  agrees with their GC SG escapee scenario. However, N-rich field stars show systematically higher O abundances compared to GC SG stars. When combined with other normal halo field stars, we can see a Na-O anti-correlation for our N-rich field stars (the average  $[\text{O}/\text{Fe}]$  is 0.11 dex lower in the stars with  $[\text{Na}/\text{Fe}] > 0.2$  compared to those with  $[\text{Na}/\text{Fe}] < 0.2$ ).

**Mg & Al:** The existence of Mg-Al anti-correlation in GCs indicates the activation of MgAl cycle (Fig.2b). Based on the FG/SG star definition by their locations on the Na-O plane, part of the SG stars are not enriched in  $[\text{Al}/\text{Fe}]$ , which is comparable to other FG stars and MW field stars. This is caused by the absence of Al enhancement in metal-rich GC stars (Pancino et al. 2017; Mészáros et al. 2020). Meanwhile, about half of the N-rich field stars show  $[\text{Al}/\text{Fe}] < +0.5$  dex, similar to the

Al-normal SG stars and MW field stars. The overall distribution of our N-rich sample shows close resemblance to that of GC SG sample, again supporting their GC SG escapee scenario.

**$\alpha$ -elements:** GC MPs affect not only Mg, but also Si among  $\alpha$ -elements, particularly in massive or metal-poor GCs (Carretta et al. 2009a; Tang et al. 2018). Apart from GC enrichment, the  $[\alpha/\text{Fe}] - [\text{Fe}/\text{H}]$  planes generally reflect the enrichment history of different galaxies (Fig.3), where SNe Ia start at lower metallicities, causing lower  $[\alpha/\text{Fe}]$  ratios in dwarf galaxies, e.g, Sculptor (Scl) and Sagittarius (Sgr) dwarf galaxies. Thus, the alpha-to-iron abundance ratios may help decipher the galaxy origins of N-rich field stars (see Section 3.2).

**Cu & Zn:** Cu is one of the odd-Z elements with metallicity-dependent yields, thus  $[\text{Cu}/\text{Fe}]$  show an increasing trend toward higher metallicities (Fig.4a), similar to the galactic evolution of Na and Al (Kobayashi

et al. 2020). However, Cu does not participate in the high-temperature hydrogen burning, therefore we do not expect variations in this element. Meanwhile, Zn is produced mainly through explosive Si burning in core-collapse supernovae. However, the increasing  $[\text{Zn}/\text{Fe}]$  of halo stars (magenta dots) toward lower metallicities (Fig.4b) indicates that a large fraction of hypernovae is needed in this region (Nomoto et al. 2013). The N-rich field stars generally follow the  $[\text{Cu}/\text{Fe}]$  (and  $[\text{Zn}/\text{Fe}]$ ) trend of other field stars. Interestingly,  $[\text{Zn}/\text{Fe}]$  abundances of dwarf galaxies are systematically lower compared to other MW field stars (Skúladóttir et al. 2017) in the metallicity range of  $[-2.0, -1.0]$ , which helps to discriminate their progenitor galaxies in Section 3.2.

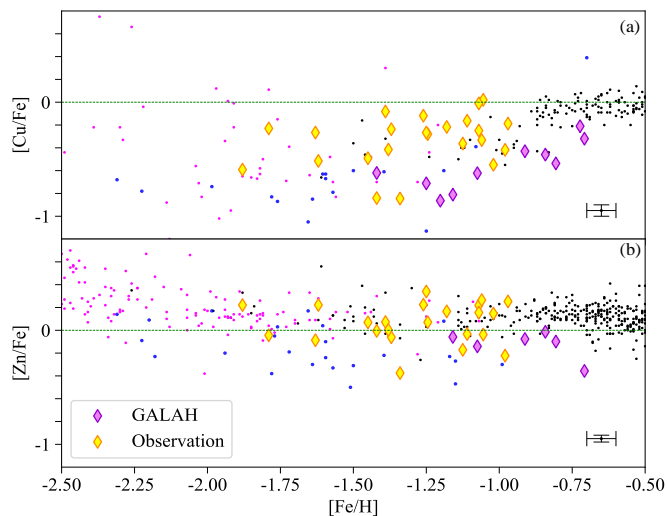


**Figure 4.** The  $[\text{Cu}/\text{Fe}]$  and  $[\text{Zn}/\text{Fe}]$  vs.  $[\text{Fe}/\text{H}]$  planes. Blue circles correspond to stars from dwarf galaxies (Sagittarius, Sculptor, Fornax, Carina and Leo I) (Hasselquist et al. 2017; Hill et al. 2019; Shetrone et al. 2003). Other symbols are the same as Fig.3.

In summary, our N-rich field stars exhibit O, Na, Mg, and Al abundance distributions similar to those of GC SG stars. Meanwhile, their Si and Ca abundances fall within the typical GC ranges. This overall pattern is consistent with the GC escapee scenario. We did not further compare chemical abundances of the iron-peak elements and neutron-capture elements between N-rich field stars and GC stars, since most GC stars do not show variation in these elements (except a few Type II GCs). GC stars generally show similar chemical abundances in these elements compared to MW field stars. And so do N-rich field stars (Yu et al. 2021).

The obvious scatters in light and  $\alpha$  elements, partial chemical kinship with dwarf galaxies yet kinematic assimilation into the halo, indicate these stars are likely to originate from different globular clusters either accreted

from dwarf satellites or formed in the Milky Way. To test whether these chemical groups trace distinct progenitor systems, we performed orbital analysis in the next subsection.

### 3.2. Chemodynamical grouping

Since the GC origins of N-rich field stars are supported by their light and  $\alpha$  elements, is it possible to identify their host GCs as in-situ or accreted? Given that  $\sim 80\%$  of GC escapees are lost to the field through tidal evaporation (Weatherford et al. 2023), most of the N-rich field stars should maintain similar kinematics as their host GCs. Moreover, the heavier element abundances are likely to be homogeneous among GCs, except for a few type II clusters (Milone et al. 2017). Assuming similar chemodynamical features between N-rich field stars, host GCs, and progenitor galaxies (Massari et al. 2019; Lin et al. 2025), studying the dynamics and chemistry of N-rich field stars may help us to obtain information about their origins.

In this work, the orbital parameters (including orbital energy  $E$ , angular momentum  $L$ , eccentricity  $e$ , inclination  $i$ ) of all stars were calculated with the publicly available Python library GALPY (Bovy 2015). Specifically,  $e = \frac{r_{apo} - r_{peri}}{r_{apo} + r_{peri}}$ , and  $i = \arccos(L_z/L)$ , where  $r_{apo}$  and  $r_{peri}$  are the apocenter radius and pericenter radius, respectively. We adopted the steady-state and axisymmetric builtin MW potential: MWpotential2014<sup>2</sup>. The values of the solar Galactocentric radius and the local circular velocity are set to  $R_\odot = 8$  kpc,  $v_\odot = 220$  km  $s^{-1}$ , respectively (Bovy et al. 2012). The peculiar velocity ( $[U_\odot, V_\odot, W_\odot]$ ) of the Sun is set to  $[11.1, 12.24, 7.25]$  km  $s^{-1}$  (Schönrich et al. 2010). The adopted distances of 23 LAMOST-identified N-rich stars are Bayesian spectrophotometric distances with no assumptions about the underlying populations (Tang et al. 2020), while STARHORSE (Queiroz et al. 2018) distances are adopted for the GALAH/APOGEE stars. We also analyzed the orbital parameters of more than five thousand MW stars selected from the GALAH DR4 catalog crossmatched with APOGEE DR17 and limited the sample to stars with a radial velocity error (from APOGEE) smaller than  $0.2$  km  $s^{-1}$  and  $RV_{scatter} < 1$  km  $s^{-1}$  (the main purpose for this selection is to ensure the accuracy of astrometry and the reliability of subsequent Galpy orbital analysis).

We divided our sample stars into two groups (Fig.5) according to their positions in  $E$ - $L_z$  phase space<sup>3</sup>.

<sup>2</sup> Switching to newer MW potential, like the one in McMillan (2017), does not significantly change our results.

<sup>3</sup> The boundary is based on that of Belokurov & Kravtsov (2024).

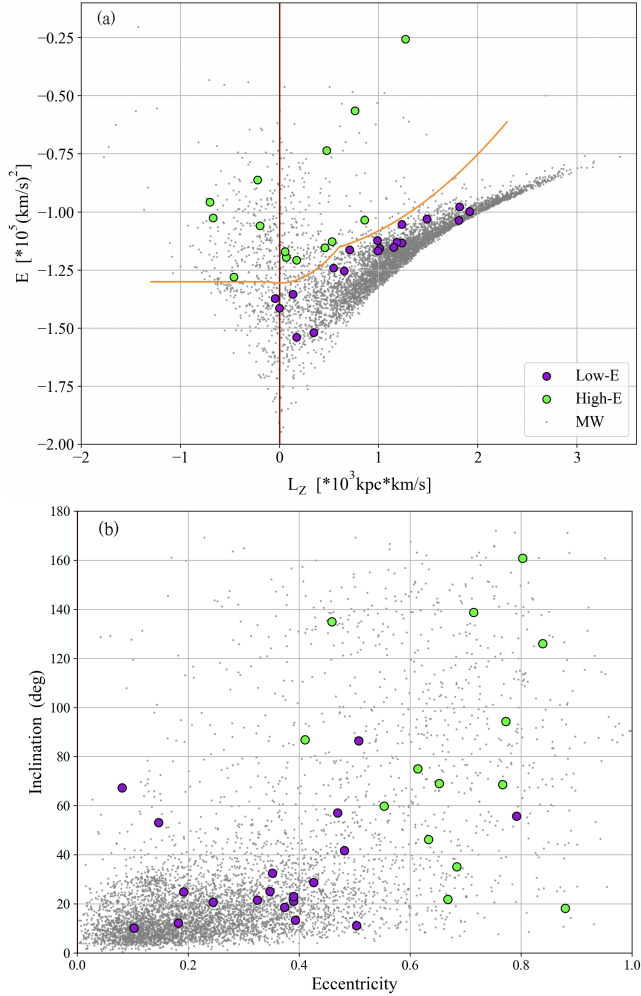


**Figure 5.** Panel a: The diagram of  $E$  vs  $L_z$  of N-rich stars (circles) in two groups and GALAH MW stars (gray dots). HE stars are colored lime and LE stars are dark violet, and the dark orange line shows the boundary between them. See text for more details about their classification. Panel b: The stars’ distribution in orbital inclination and eccentricity.

(1) High-Energy group (High-E group, or HE): These stars generally exhibit higher orbital energies ( $E$ ) and high eccentricities. Their dynamics align with known accreted structures like the Gaia-Sausage-Enceladus (GSE, [Horta et al. 2021](#)). (2) Low-Energy group (Low-E group, or LE): These stars generally show lower orbital energies, mostly positive  $L_z$ , smaller inclination angles, and lower eccentricities. Their dynamical similarity to the MW thick disk stars implies in-situ origins. In order to compare the chemical abundances of these two groups, it is optimal to use an overlapping metallicity range. After balancing the bin sizes and sample sizes, we divided each group into two with  $[\text{Fe}/\text{H}] = -1.1$  as the boundary, so there are 4 subgroups: high-energy metal-poor (HE-MP), low-energy metal-poor (LE-MP), high-

energy metal-rich (HE-MR), and low-energy metal-rich (LE-MR). Their mean metallicities are  $-1.38 \pm 0.186$ ,  $-1.38 \pm 0.232$ ,  $-1.02 \pm 0.039$ ,  $-0.94 \pm 0.134$ , respectively. Such partitioning allows targeted investigation of how birth GC environments (accreted vs. in-situ) imprint distinct chemical signatures on their escaped stars. The systematic abundance differences between high-energy (HE) and low-energy (LE) N-rich stars (Figs. 6 & 7 & 8) provide critical insights into their distinct progenitor environments and Galactic assembly history.

$\alpha$  elements: As we mentioned earlier in Section 3.1, stars born in dwarf galaxies generally show lower  $[\alpha/\text{Fe}]$  compared to in-situ stars at  $[\text{Fe}/\text{H}] \gtrsim -1.5$ . Assuming HE stars are mostly accreted, while LE stars are mostly in-situ, we expect lower  $[\alpha/\text{Fe}]$  for HE stars compared to LE stars. This agrees with the observations in Fig. 6, except for Ca and Ti in the metal-rich region. Such exception may be caused by two reasons: (1) Accreted (especially from GSE) and in-situ stars show smaller differences in  $[\text{Ca}/\text{Fe}]$  and  $[\text{Ti}/\text{Fe}]$  at a given metallicity ([Hasselquist et al. 2021](#)); (2) HE-MR stars are on average more metal-poor than LE-MR stars ( $-1.02 \pm 0.039$  versus  $-0.94 \pm 0.134$ ). We also note that HE and LE stars show smaller  $[\alpha/\text{Fe}]$  differences for MP groups, since in-situ stars and accreted stars show similar  $[\alpha/\text{Fe}]$  at  $[\text{Fe}/\text{H}] < -1.5$ , and the abundances of Mg and Si are possibly affected more obviously by H-burning in metal-poor GC environments.

Iron-peak elements: Sc, V, Cr, Mn, Co, and Ni are substantially generated by SNe Ia, thus showing close correlations with Fe. HE and LE stars do not show significant differences in these elements, except for Mn and Co in the metal-rich regime. Such exception may be caused by the lower production of Mn and Co in SNe Ia of dwarf galaxies ([Sanders et al. 2021](#); [Yu et al. 2021](#)). Contrary to our results, [Nissen & Schuster \(2010\)](#) and [Fishlock et al. \(2017\)](#) suggested that in-situ and accreted populations show nontrivial differences in  $[\text{Ni}/\text{Fe}]$  and  $[\text{Sc}/\text{Fe}]$ . Admittedly, the lower spectral resolution and lower SNR in our work compared to theirs result in lower precision (0.1 dex vs. 0.01 dex), possibly causing the non-detection of Sc and Ni differences between the two sub-populations.

Cu & Zn: In the primordial MW where rapid star formation and frequent Type II SNe enhanced Zn production via  $\alpha$ -rich freeze-out, while earlier SN Ia contributions suppressed Zn enrichment in dwarf galaxies. On the other hand, Cu in nearby dwarf spheroidal galaxies show similar abundances as MW halo stars ([Shetrone et al. 2003](#)). In this work, we find that HE and LE groups show similar  $[\text{Cu}/\text{Fe}]$  values within the uncertainty ranges. Different from Cu, LE stars exhibit

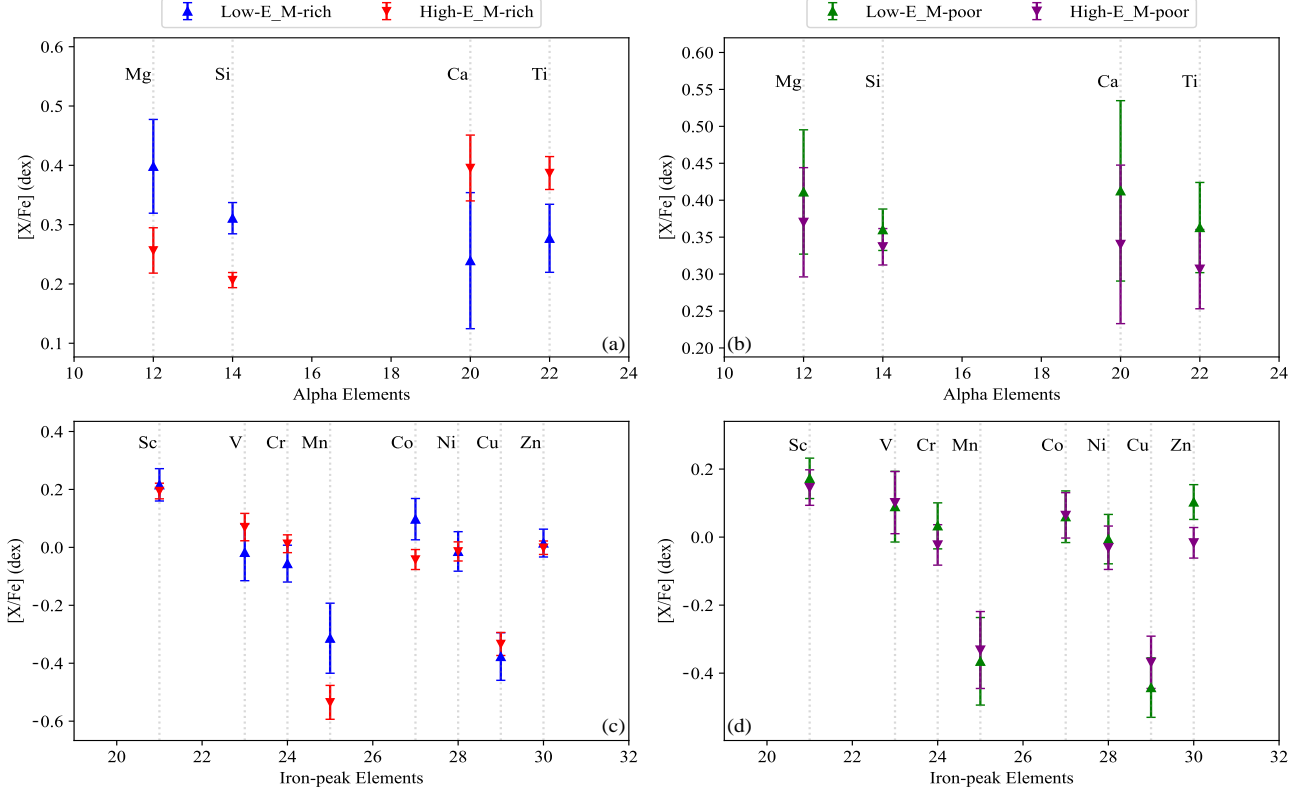


**Figure 6.** The chemical patterns of different groups, including  $\alpha$  elements, iron-peak elements, Cu and Zn. Triangles stand for the average element abundances of 4 groups with corresponding errors (blue for LE-MR, red for HE-MR, green for LE-MP and purple for HE-MP).

higher  $[Zn/Fe]$  than HE stars in MP groups ( $\Delta \sim 0.15$  dex), consistent with the in-situ formation feature. Conversely, HE stars' lower  $[Zn/Fe]$  agree with other dwarf galaxies (Skúladóttir et al. 2017; Shetrone et al. 2003).

**Neutron-capture elements:** The systematic differences in neutron-capture element abundances ( $[X/Eu]$ ) between high-energy (HE) and low-energy (LE) nitrogen-rich stars are illustrated in Fig.7 and provide specific clues to their origins and the Milky Way's assembly history. HE stars exhibit lower  $[Y/Eu]$ ,  $[Zr/Eu]$ , and  $[Ba/Eu]$  ratios compared to LE stars, reflecting a dominance of  $r$ -process nucleosynthesis over the  $s$ -process. Besides the  $[X/Eu]$  ratios displayed, HE stars also show a higher mean  $[La/Zr]$  ratio and lower mean  $[Zr/Fe]$ , consistent with the chemical pattern of low- $\alpha$  sample studied in Fishlock et al. (2017). This pattern arises because HE stars likely formed in massive dwarf galaxies (e.g., the Gaia-Sausage-Enceladus remnant), where core-collapse supernovae and delayed neutron star mergers significantly contributed to the nearly pure  $r$ -process enrichment (Snedden et al. 2008; Naidu et al. 2022). In contrast, LE stars, presumably associated with the in-situ populations, show enhanced  $[X/Eu]$ ,  $[Zr/Fe]$  and lower  $[La/Zr]$  due to prolonged contributions from AGB stars, which efficiently produce  $s$ -

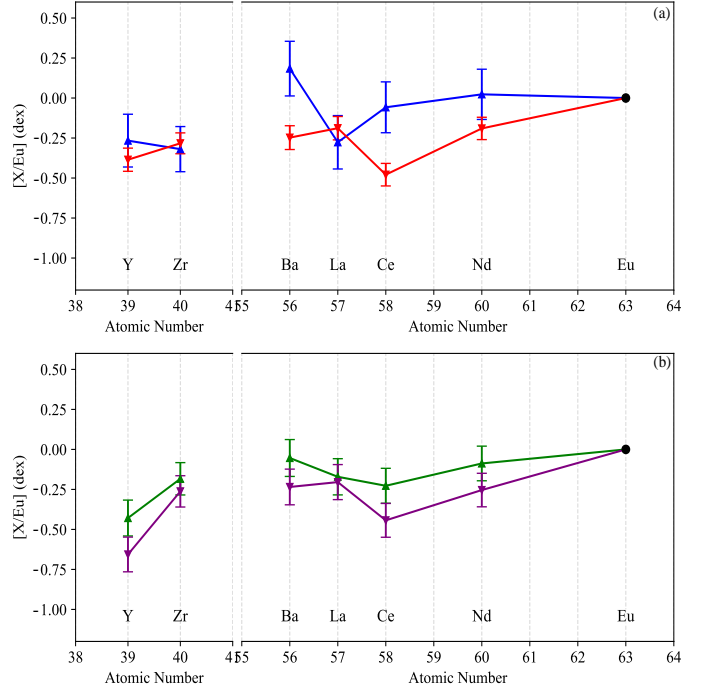


**Figure 7.** The chemical patterns of neutron-capture elements of different groups in the form of  $[X/Eu]$ . Markers are the same as Fig.6.

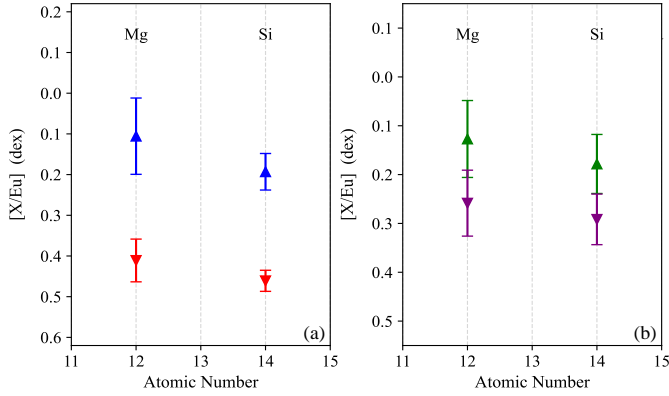


**Figure 8.**  $[\text{Mg}/\text{Eu}]$  and  $[\text{Si}/\text{Eu}]$  of different groups. Markers are the same as Fig.6.

process elements (Karakas & Lattanzio 2014; Kobayashi et al. 2020). Moreover, we find that the LE stars exhibit systematically higher mean  $[\alpha/\text{Eu}]$  (using Mg and Si as  $\alpha$ -element representatives) than the HE stars across both metal-poor and metal-rich regimes (see Fig.8). This pattern aligns with established results where accreted stars (like GSE remnants) show elevated  $[\text{Eu}/\alpha]$  compared to MW in-situ stars (Matsuno et al. 2021; Monty et al. 2024). On the whole, the persistence of low  $[\text{X}/\text{Eu}]$  and other features mentioned in HE groups support our chemodynamical inference, underscoring their distinct accretion origin independent of in-situ galactic chemical evolution. These findings align with hierarchical galaxy formation models, where the MW incorporated chemically distinct populations via mergers, as evidenced by dynamical studies linking HE kinematics to disrupted massive satellites (Ji et al. 2016; Helmi et al. 2018).

In conclusion, the observed discrepancies between HE and LE stars collectively suggest a dichotomy in their chemodynamical properties, pointing to distinct progenitor environments. HE stars might have been escaped from GCs belonging to disrupted dwarf galaxies, where the enrichment processes were less efficient or occurred over a longer timescale. Conversely, LE stars, which are more likely to be GC escapees confined to the MW disk reflecting a history of sustained chemical enrichment.

## 4. DISCUSSION

### 4.1. Connection between N-rich field stars and high-redshift N-emitters

After the launch of JWST, astronomers are reevaluating the scientific significance of GCs in the high-redshift Universe. Observations now indicate their dominant role on galaxy evolution at these redshifts. Clumpy and bursty star formation on parsec scale ob-

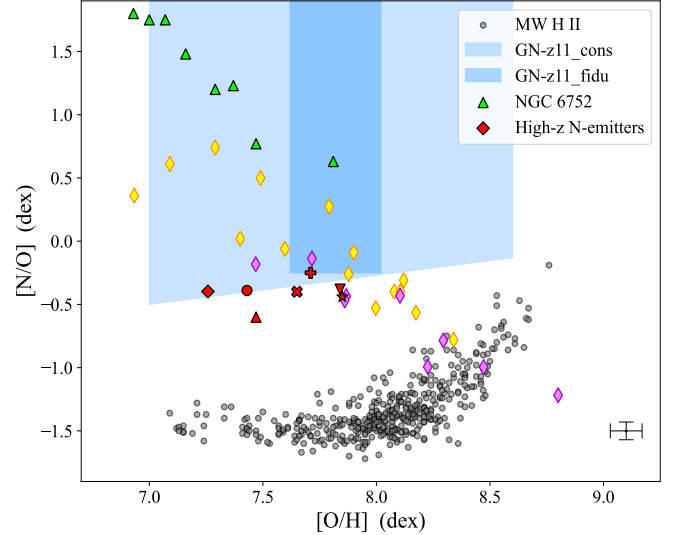


**Figure 9.** The  $[\text{N}/\text{O}] - [\text{O}/\text{H}]$  plane. Small gray circles show the Galactic H II region abundances from Pilyugin et al. (2012). The conservative (fiducial) range of  $[\text{N}/\text{O}]$  and  $[\text{O}/\text{H}]$  inferred for GN-z11 from Cameron et al. (2023) is displayed as the light (dark) dodgerblue shaded region. Values for high-z N-emitters (Senchyna et al. 2024; Navarro-Carrera et al. 2024; Senchyna et al. 2017; Isobe et al. 2023; Topping et al. 2024, 2025) are shown as red markers and lime triangles are measurements from stars in NGC 6752 (Carretta et al. 2005).

served at high redshift ( $z \sim 8 - 11$ ) suggests that these are proto-GC actively forming (e.g., Marques-Chaves et al. 2024). Furthermore, newly discovered “N-emitters” exhibiting  $[\text{N}/\text{O}]$  ratios similar to stars in local GCs, indicating they might be also forming GCs (e.g., Topping et al. 2024, 2025).

In this work, we show that N-rich field stars are possible candidates of GC escaped stars. Do they show similar  $[\text{N}/\text{O}]$  ratios as those high-redshift N-emitters or local GCs? To investigate their connections, we compared their  $[\text{N}/\text{O}]$  vs.  $[\text{O}/\text{H}]$  ratios in Fig.9, including local H II regions for reference. Our sample stars reveal an anti-correlation between  $[\text{N}/\text{O}]$  and  $[\text{O}/\text{H}]$ , a trend also observed in stars within the GC NGC 6752. Most N-rich field stars occupy the same region in this plane as high-redshift N-emitters, implying a similar enrichment history. Exceptions occur among the more metal-rich N-rich field stars ( $[\text{Fe}/\text{H}] \gtrsim -1.0$ ), whose  $[\text{N}/\text{O}]$  ratios align more closely to local H II regions. This chemical pattern suggest that N-rich field stars with  $[\text{Fe}/\text{H}] \lesssim -1.0$  are local analogs of the high-redshift N-emitters. On the contrary, N-rich field stars with  $[\text{Fe}/\text{H}] > -1.0$  may not have similar chemical enrichment mechanism as N-emitters. Consequently, these findings support the validity of the metallicity cut ap-

plied to LAMOST-identified N-rich field stars (Tang et al. 2019, 2020).

#### 4.2. Tracing origins among globular clusters

The concurrent spatial proximity and chemical coherence between nitrogen-enhanced field stars and specific GCs provide most compelling evidence for dynamical escape scenarios (e.g., Souza et al. 2024; Huang et al. 2025). In this work, we have attempted to provide direct evidence linking the N-rich stars to their possible host GCs. We calculated the orbital elements of more than 100 known GCs using the kinematic parameters reported in Baumgardt et al. (2019), and for each specific N-rich star we selected candidate GCs which are relatively similar to it in the  $E$ - $L_z$  phase space (Xu et al. 2024). Then we performed orbit integrations of both the stars and candidate GCs with Galpy to see if they would get close in space while tracing back. Among all the matching results, the most representative pair is star Num28 and NGC 6235. Orbit integrations revealed a close encounter in space ( $< 0.1$  kpc, comparable to the typical tidal radii of GCs) between them about 380 Myrs ago (panel a & b of Fig.10). To explore the effect of orbital uncertainties, we applied a Monte Carlo analysis of the orbit integration. We performed 1000 orbit integrations by randomly perturbing the proper motions and distances of Num28 and NGC 6235. These parameters were drawn from normal distributions with  $\sigma_1 = 0.02$  mas yr $^{-1}$  for  $\mu_{\alpha*}$  and  $\mu_{\delta}$ ,  $\sigma_2 = 0.2$  kpc for distance around the measured values. The results revealed that in about 36% of the simulations, the minimum separation distance between Num28 and NGC 6235 during the integration was smaller than 0.3 kpc (panel c of Fig.10).

This evidence about orbits encounter is part of a combined chemodynamical argument, which includes not only kinematic consistency in  $E$ - $L_z$  space but also chemical similarity. The  $[\text{Fe}/\text{H}]$  of star Num28 matches that of NGC 6235 ( $\sim -1.1$  dex) (Howland et al. 2003) within 0.1 dex and the light-element abundances indicate that Star Num28 is an SG star with enhanced N, Na, and Al ( $[\text{N}/\text{Fe}] = 1.09$ ,  $[\text{Na}/\text{Fe}] = 0.71$ ,  $[\text{Al}/\text{Fe}] = 0.53$ ). The close encounter between star Num28 and NGC 6235, is intriguing given their high relative velocity ( $> 300$  km s $^{-1}$ ). This high speed is difficult to explain through standard tidal stripping alone and suggests a more violent ejection mechanism. One probable scenario is that Num28 experienced a gravitational “kick” from an intermediate-mass black hole within the cluster, which would impart the high velocity required for escape, providing a dynamic alternative to the gradual stripping of stars (Huang et al. 2025). These combined chemodynamical analysis suggest that star Num28 is a

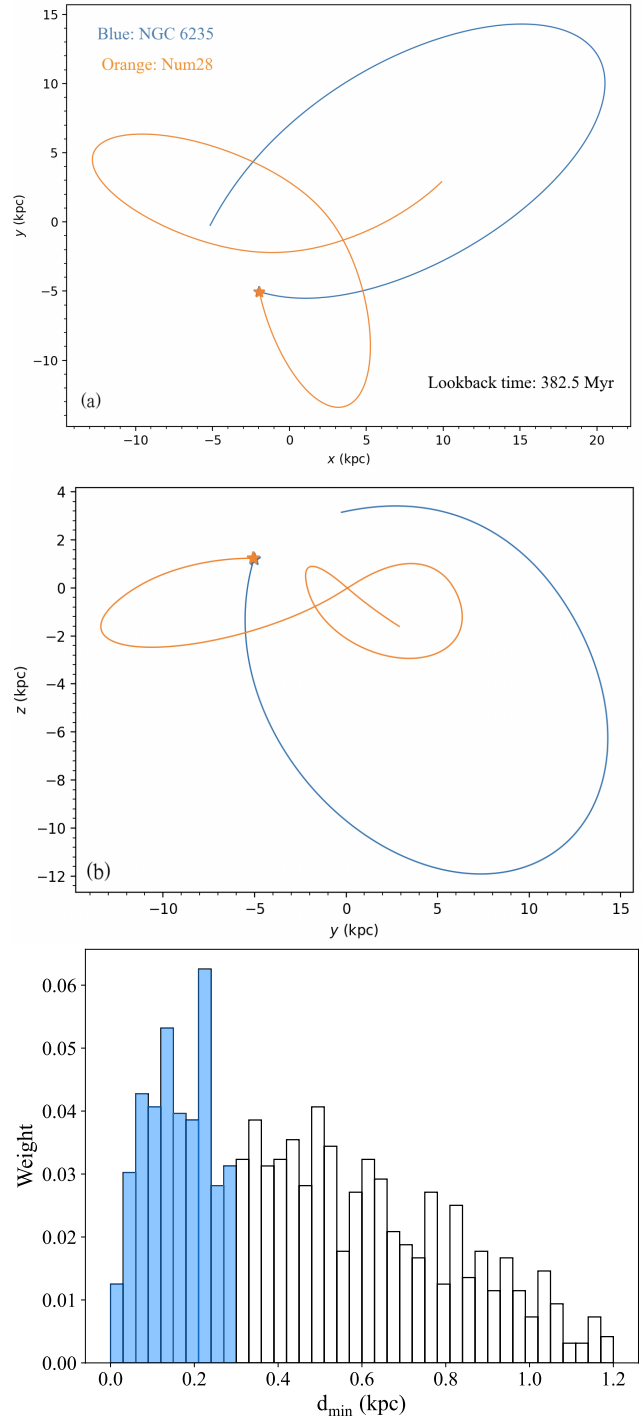


**Figure 10.** Panel a & b: Orbital integrations of NGC 6235 and Star Num28. Filled stars stand for their spatial locations at the look-back time and lines indicate their orbits (dodger blue for NGC 6235 and orange for Num28). Panel c: The distribution of minimum distances between the integrated orbits of Num28 and NGC 6235 revealed by the Monte Carlo analysis.

likely SG escapee from NGC 6235, contributing to our understanding of globular cluster dissolution and the Galactic stellar halo’s origins.

Meanwhile, uncertainties persist. The orbital encounter rate reflects the sensitivity of long-term orbital integration to distance uncertainties, therefore, improving distance precision is a key to enable more robust investigations in the future. Also, assumptions in Galactic potential models and others may influence orbit reconstruction. Future studies should prioritize high-precision astrometry, such as upcoming Gaia data releases, to test the robustness of the association. By transforming N-rich stars from chemical curiosities into quantitative probes, this work may provide a template for reconstructing the Milky Way’s hierarchical assembly — one escaped star at a time.

## 5. SUMMARY

This study establishes nitrogen-enhanced field stars as definitive tracers of globular cluster (GC) disruption and Galactic accretion by synthesizing orbital dynamics and multi-element chemical abundances. This work is part of our ongoing research project, “Scrutinizing GALaxy-STaR cluster coevolutiON with chemODynaMIcs (GASTRONOMI)”, which leverages multi-wavelength photometric and spectroscopic data to unravel the coevolutionary relationships between the MW, its satellite dwarf galaxies, and their star clusters. Using high-resolution spectroscopy of ESPaDOnS, MIKE and GALAH for 33 N-rich stars, we analyzed their chemodynamical features and confirmed evident chemical similarity in multi-element abundances between these stars and the GC second generation stars, reinforcing the association between N-rich field stars and globular clusters.

To explore the possible formation pathways, we classified the stars into different groups according to orbital energy and metallicity. HE groups exhibit orbital parameters aligning with accreted massive dwarf galaxies, like GSE, meanwhile, LE groups show disk-like kinematics consistent with in-situ populations. And their distinct chemical patterns suggest different progenitor environments: HE groups trace clusters stripped from massive dwarf galaxies with enhanced r/s-process ratios, and LE groups are likely to originate from GCs formed within the Milky Way, enhanced in  $\alpha$  elements relative to their counterparts formed in dwarf galaxies and accreted into MW.

We also found a chemical connection between metal-poor Milky Way N-rich field stars and high-redshift “N-emitters.” They occupy the same region in the [N/O] vs. [O/H] plane, suggesting a similar enrichment history

and indicating that the local N-rich stars are analogs of the high-z systems, possibly linked to globular cluster formation. Furthermore, using orbital integration, we traced possible second generation stars of peculiar globular clusters and this method can be applied to larger samples with more accurate stellar distances.

These results help resolve long-standing ambiguities in N-rich field stars’ origins: their chemodynamical clustering decouples accretion signatures from in-situ disruption. All in all, these cases collectively transform single-star archaeology into a tool for reconstructing cluster dissolution histories.

There are still critical avenues demanding exploration in the future. Current samples lack metal-poor stars ( $[\text{Fe}/\text{H}] < -2.0$  dex), where pristine accretion signatures may dominate. High-resolution UV spectroscopy is essential to measure the abundances of CNO and *r*-process elements in this metallicity regime. Measurements of CNO are crucial as they directly probe the proton-capture processes unique to the multiple populations within GCs. Neutron-capture elements, especially *r*-process elements which are more difficult to measure, serve as tracers to distinguish whether the ancestral systems formed in-situ or were accreted with distinct chemical evolution histories. Another problem is the limited multi-element data, especially for the neutron-capture elements. Future surveys (e.g., 4MOST, WEAVE) will provide more Eu/Ba/La/Ce measurements for chemical peculiar stars to map *r*/*s*-process cartography in accreted systems. There is no doubt that larger samples available and more comprehensive chemical abundance data will provide crucial assistance for the studies of Galactic archaeology with chemical peculiar stars.

## ACKNOWLEDGMENTS

Y. Qiao, B. Tang gratefully acknowledge support from the National Natural Science Foundation of China through grants NOs. 12233013 and 12473035, China Manned Space Project under grant NO. CMS-CSST-2025-A13 and CMS-CSST-2021-A08, the Fundamental Research Funds for the Central Universities, Sun Yat-sen University (24qny121). J.G.F-T gratefully acknowledges the grants support provided by ANID Fondecyt Postdoc No. 3230001 (Sponsoring researcher), the Joint Committee ESO-Government of Chile under the agreement 2023 ORP 062/2023, and the support of the Doctoral Program in Artificial Intelligence, DISC-UCN. C. Allende Prieto acknowledges financial support from the Spanish Ministry of Science, Innovation and Universities (MICIU) projects PID2020-117493GB-I00, PID2023-149982NB-I00 and PID2023-146453NB-I00 (*PLAtoSOnG*). B. Barbuy acknowledges partial financial support from FAPESP, CNPq, and CAPES. T. Masseron acknowledge support from the Spanish Ministry of Science and Innovation with the grant No. PID2023-146453NB-100 (*PLAtoSOnG*). Z. Y. is supported by the National Key R&D Program of China via 2024YFA1611601.

*Software:* TOPCAT (Taylor 2005), BACCHUS (Masseron et al. 2016), iSpec (Vosegaard 2018), PySME (Wehrhahn 2021), Matplotlib (Hunter 2007), Numpy (Van der Walt et al. 2011; Harris et al. 2020), Math, Pandas (McKinney 2010), Astropy (Astropy Collaboration et al. 2013, 2018), Scipy (Virtanen et al. 2020), Seaborn (Waskom 2021), Telluric-Filter, Galpy (Bovy 2015), StarHorse (Queiroz et al. 2018).

## REFERENCES

- Antoja, T., Helmi, A., Romero-Gómez, M., et al. 2018, *Nature*, 561, 360, doi: [10.1038/s41586-018-0510-7](https://doi.org/10.1038/s41586-018-0510-7)
- Arnould, M., Goriely, S., & Jorissen, A. 1999, *A&A*, 347, 572, doi: [10.48550/arXiv.astro-ph/9904407](https://doi.org/10.48550/arXiv.astro-ph/9904407)
- Astropy Collaboration, Robitaille, T. P., Tollerud, E. J., et al. 2013, *A&A*, 558, A33, doi: [10.1051/0004-6361/201322068](https://doi.org/10.1051/0004-6361/201322068)
- Astropy Collaboration, Price-Whelan, A. M., Sipőcz, B. M., et al. 2018, *AJ*, 156, 123, doi: [10.3847/1538-3881/aabc4f](https://doi.org/10.3847/1538-3881/aabc4f)
- Barklem, P. S., Christlieb, N., Beers, T. C., et al. 2005, *A&A*, 439, 129, doi: [10.1051/0004-6361:20052967](https://doi.org/10.1051/0004-6361:20052967)
- Bastian, N., & Lardo, C. 2018, *ARA&A*, 56, 83, doi: [10.1146/annurev-astro-081817-051839](https://doi.org/10.1146/annurev-astro-081817-051839)
- Baumgardt, H., Hilker, M., Sollima, A., & Bellini, A. 2019, *MNRAS*, 482, 5138, doi: [10.1093/mnras/sty2997](https://doi.org/10.1093/mnras/sty2997)
- Baumgardt, H., & Makino, J. 2003, *MNRAS*, 340, 227, doi: [10.1046/j.1365-8711.2003.06286.x](https://doi.org/10.1046/j.1365-8711.2003.06286.x)
- Beers, T. C., Carollo, D., Ivezić, Ž., et al. 2012, *ApJ*, 746, 34, doi: [10.1088/0004-637X/746/1/34](https://doi.org/10.1088/0004-637X/746/1/34)
- Belokurov, V., Erkal, D., Evans, N. W., Koposov, S. E., & Deason, A. J. 2018, *MNRAS*, 478, 611, doi: [10.1093/mnras/sty982](https://doi.org/10.1093/mnras/sty982)
- Belokurov, V., & Kravtsov, A. 2024, *MNRAS*, 528, 3198, doi: [10.1093/mnras/stad3920](https://doi.org/10.1093/mnras/stad3920)
- Bensby, T., Feltzing, S., & Oey, M. S. 2014, *A&A*, 562, A71, doi: [10.1051/0004-6361/201322631](https://doi.org/10.1051/0004-6361/201322631)
- Bernstein, R., Shtetman, S. A., Gunnels, S. M., Mochnacki, S., & Athey, A. E. 2003, in *Society of Photo-Optical Instrumentation Engineers (SPIE) Conference Series*, Vol. 4841, *Instrument Design and Performance for Optical/Infrared Ground-based Telescopes*, ed. M. Iye & A. F. M. Moorwood, 1694–1704, doi: [10.1117/12.461502](https://doi.org/10.1117/12.461502)
- Blanco-Cuaresma, S., Soubiran, C., Heiter, U., & Jofré, P. 2014, *A&A*, 569, A111, doi: [10.1051/0004-6361/201423945](https://doi.org/10.1051/0004-6361/201423945)
- Blanton, M. R., Bershady, M. A., Abolfathi, B., et al. 2017, *AJ*, 154, 28, doi: [10.3847/1538-3881/aa7567](https://doi.org/10.3847/1538-3881/aa7567)
- Bovy, J. 2015, *ApJS*, 216, 29, doi: [10.1088/0067-0049/216/2/29](https://doi.org/10.1088/0067-0049/216/2/29)
- Bovy, J., Allende Prieto, C., Beers, T. C., et al. 2012, *ApJ*, 759, 131, doi: [10.1088/0004-637X/759/2/131](https://doi.org/10.1088/0004-637X/759/2/131)
- Buder, S., Kos, J., Wang, X. E., et al. 2025, *PASA*, 42, e051, doi: [10.1017/pasa.2025.26](https://doi.org/10.1017/pasa.2025.26)

- Cameron, A. J., Saxena, A., Bunker, A. J., et al. 2023, *A&A*, 677, A115, doi: [10.1051/0004-6361/202346107](https://doi.org/10.1051/0004-6361/202346107)
- Carollo, D., Beers, T. C., Chiba, M., et al. 2010, *ApJ*, 712, 692, doi: [10.1088/0004-637X/712/1/692](https://doi.org/10.1088/0004-637X/712/1/692)
- Carretta, E., Bragaglia, A., Gratton, R., & Lucatello, S. 2009a, *A&A*, 505, 139, doi: [10.1051/0004-6361/200912097](https://doi.org/10.1051/0004-6361/200912097)
- Carretta, E., Gratton, R. G., Lucatello, S., Bragaglia, A., & Bonifacio, P. 2005, *A&A*, 433, 597, doi: [10.1051/0004-6361:20041892](https://doi.org/10.1051/0004-6361:20041892)
- Carretta, E., Lucatello, S., Gratton, R. G., Bragaglia, A., & D’Orazi, V. 2011, *A&A*, 533, A69, doi: [10.1051/0004-6361/201117269](https://doi.org/10.1051/0004-6361/201117269)
- Carretta, E., Bragaglia, A., Gratton, R. G., et al. 2009b, *A&A*, 505, 117, doi: [10.1051/0004-6361/200912096](https://doi.org/10.1051/0004-6361/200912096)
- Cayrel, R., Depagne, E., Spite, M., et al. 2004, *A&A*, 416, 1117, doi: [10.1051/0004-6361:20034074](https://doi.org/10.1051/0004-6361:20034074)
- Cui, X.-Q., Zhao, Y.-H., Chu, Y.-Q., et al. 2012, *Research in Astronomy and Astrophysics*, 12, 1197, doi: [10.1088/1674-4527/12/9/003](https://doi.org/10.1088/1674-4527/12/9/003)
- Deng, L.-C., Newberg, H. J., Liu, C., et al. 2012, *Research in Astronomy and Astrophysics*, 12, 735, doi: [10.1088/1674-4527/12/7/003](https://doi.org/10.1088/1674-4527/12/7/003)
- D’Ercole, A., D’Antona, F., & Vesperini, E. 2011, *MNRAS*, 415, 1304, doi: [10.1111/j.1365-2966.2011.18776.x](https://doi.org/10.1111/j.1365-2966.2011.18776.x)
- Donati, J. F., Catala, C., Landstreet, J. D., & Petit, P. 2006, in *Astronomical Society of the Pacific Conference Series*, Vol. 358, *Solar Polarization 4*, ed. R. Casini & B. W. Lites, 362
- Fernández-Trincado, J. G., Beers, T. C., Tang, B., et al. 2019, *MNRAS*, 488, 2864, doi: [10.1093/mnras/stz1848](https://doi.org/10.1093/mnras/stz1848)
- Fernández-Trincado, J. G., Zamora, O., García-Hernández, D. A., et al. 2017, *ApJL*, 846, L2, doi: [10.3847/2041-8213/aa8032](https://doi.org/10.3847/2041-8213/aa8032)
- Fernández-Trincado, J. G., Beers, T. C., Barbuy, B., et al. 2022, *A&A*, 663, A126, doi: [10.1051/0004-6361/202243195](https://doi.org/10.1051/0004-6361/202243195)
- Fishlock, C. K., Yong, D., Karakas, A. I., et al. 2017, *MNRAS*, 466, 4672, doi: [10.1093/mnras/stx047](https://doi.org/10.1093/mnras/stx047)
- Fulbright, J. P. 2000, *AJ*, 120, 1841, doi: [10.1086/301548](https://doi.org/10.1086/301548)
- García Pérez, A. E., Allende Prieto, C., Holtzman, J. A., et al. 2016, *AJ*, 151, 144, doi: [10.3847/0004-6256/151/6/144](https://doi.org/10.3847/0004-6256/151/6/144)
- Gustafsson, B., Edvardsson, B., Eriksson, K., et al. 2008, *A&A*, 486, 951, doi: [10.1051/0004-6361:200809724](https://doi.org/10.1051/0004-6361:200809724)
- Harbeck, D., Smith, G. H., & Grebel, E. K. 2003, *AJ*, 125, 197, doi: [10.1086/345570](https://doi.org/10.1086/345570)
- Harris, C. R., Millman, K. J., van der Walt, S. J., et al. 2020, *Nature*, 585, 357, doi: [10.1038/s41586-020-2649-2](https://doi.org/10.1038/s41586-020-2649-2)
- Hasselquist, S., Shetrone, M., Smith, V., et al. 2017, *ApJ*, 845, 162, doi: [10.3847/1538-4357/aa7ddc](https://doi.org/10.3847/1538-4357/aa7ddc)
- Hasselquist, S., Hayes, C. R., Lian, J., et al. 2021, *ApJ*, 923, 172, doi: [10.3847/1538-4357/ac25f9](https://doi.org/10.3847/1538-4357/ac25f9)
- Hayes, C. R., Majewski, S. R., Hasselquist, S., et al. 2020, *ApJ*, 889, 63, doi: [10.3847/1538-4357/ab62ad](https://doi.org/10.3847/1538-4357/ab62ad)
- Helmi, A., Babusiaux, C., Koppelman, H. H., et al. 2018, *Nature*, 563, 85, doi: [10.1038/s41586-018-0625-x](https://doi.org/10.1038/s41586-018-0625-x)
- Hill, V., Skúladóttir, Á., Tolstoy, E., et al. 2019, *A&A*, 626, A15, doi: [10.1051/0004-6361/201833950](https://doi.org/10.1051/0004-6361/201833950)
- Horta, D., Schiavon, R. P., Mackereth, J. T., et al. 2021, *MNRAS*, 500, 1385, doi: [10.1093/mnras/staa2987](https://doi.org/10.1093/mnras/staa2987)
- Howland, R., Sarajedini, A., Tiede, G. P., et al. 2003, *AJ*, 125, 801, doi: [10.1086/345730](https://doi.org/10.1086/345730)
- Huang, R., Tang, B., Li, C., et al. 2024, *Science China Physics, Mechanics, and Astronomy*, 67, 259513, doi: [10.1007/s11433-023-2332-5](https://doi.org/10.1007/s11433-023-2332-5)
- Huang, Y., Li, Q., Liu, J., et al. 2025, *National Science Review*, 12, 347, doi: [10.1093/nsr/nwae347](https://doi.org/10.1093/nsr/nwae347)
- Hunter, J. D. 2007, *Computing in Science and Engineering*, 9, 90, doi: [10.1109/MCSE.2007.55](https://doi.org/10.1109/MCSE.2007.55)
- Ibata, R. A., Gilmore, G., & Irwin, M. J. 1994, *Nature*, 370, 194, doi: [10.1038/370194a0](https://doi.org/10.1038/370194a0)
- Isobe, Y., Ouchi, M., Tominaga, N., et al. 2023, *ApJ*, 959, 100, doi: [10.3847/1538-4357/ad09be](https://doi.org/10.3847/1538-4357/ad09be)
- Ji, A. P., Frebel, A., Chiti, A., & Simon, J. D. 2016, *Nature*, 531, 610, doi: [10.1038/nature17425](https://doi.org/10.1038/nature17425)
- Karakas, A. I., & Lattanzio, J. C. 2014, *PASA*, 31, e030, doi: [10.1017/pasa.2014.21](https://doi.org/10.1017/pasa.2014.21)
- Kisku, S., Schiavon, R. P., Horta, D., et al. 2021, *MNRAS*, 504, 1657, doi: [10.1093/mnras/stab525](https://doi.org/10.1093/mnras/stab525)
- Kobayashi, C., Karakas, A. I., & Lugaro, M. 2020, *ApJ*, 900, 179, doi: [10.3847/1538-4357/abae65](https://doi.org/10.3847/1538-4357/abae65)
- Krause, M. G. H., Charbonnel, C., Bastian, N., & Diehl, R. 2016, *A&A*, 587, A53, doi: [10.1051/0004-6361/201526685](https://doi.org/10.1051/0004-6361/201526685)
- Lagarde, N., Decressin, T., Charbonnel, C., et al. 2012, *A&A*, 543, A108, doi: [10.1051/0004-6361/201118331](https://doi.org/10.1051/0004-6361/201118331)
- Laporte, C. F. P., Belokurov, V., Koposov, S. E., Smith, M. C., & Hill, V. 2020, *MNRAS*, 492, L61, doi: [10.1093/mnrasl/slz167](https://doi.org/10.1093/mnrasl/slz167)
- Lin, S., Tang, B., Liu, G., et al. 2025, *ApJL*, 989, L37, doi: [10.3847/2041-8213/adf748](https://doi.org/10.3847/2041-8213/adf748)
- Lind, K., Koposov, S. E., Battistini, C., et al. 2015, *A&A*, 575, L12, doi: [10.1051/0004-6361/201425554](https://doi.org/10.1051/0004-6361/201425554)
- Majewski, S. R., Skrutskie, M. F., Weinberg, M. D., & Ostheimer, J. C. 2003, *ApJ*, 599, 1082, doi: [10.1086/379504](https://doi.org/10.1086/379504)
- Marques-Chaves, R., Schaerer, D., Kuruvanthodi, A., et al. 2024, *A&A*, 681, A30, doi: [10.1051/0004-6361/202347411](https://doi.org/10.1051/0004-6361/202347411)

- Martell, S. L., Smolinski, J. P., Beers, T. C., & Grebel, E. K. 2011, *A&A*, 534, A136, doi: [10.1051/0004-6361/201117644](https://doi.org/10.1051/0004-6361/201117644)
- Martell, S. L., Shetrone, M. D., Lucatello, S., et al. 2016, *ApJ*, 825, 146, doi: [10.3847/0004-637X/825/2/146](https://doi.org/10.3847/0004-637X/825/2/146)
- Massari, D., Koppelman, H. H., & Helmi, A. 2019, *A&A*, 630, L4, doi: [10.1051/0004-6361/201936135](https://doi.org/10.1051/0004-6361/201936135)
- Masseron, T., Merle, T., & Hawkins, K. 2016, BACCHUS: Brussels Automatic Code for Characterizing High accuracy Spectra, Astrophysics Source Code Library, record ascl:1605.004
- Matsuno, T., Hirai, Y., Tarumi, Y., et al. 2021, *A&A*, 650, A110, doi: [10.1051/0004-6361/202040227](https://doi.org/10.1051/0004-6361/202040227)
- McKinney, W. 2010, in Proceedings of the 9th Python in Science Conference, ed. Stéfan van der Walt & Jarrod Millman, 56 – 61, doi: [10.25080/Majora-92bf1922-00a](https://doi.org/10.25080/Majora-92bf1922-00a)
- McMillan, P. J. 2017, *MNRAS*, 465, 76, doi: [10.1093/mnras/stw2759](https://doi.org/10.1093/mnras/stw2759)
- Mészáros, S., Masseron, T., García-Hernández, D. A., et al. 2020, *MNRAS*, 492, 1641, doi: [10.1093/mnras/stz3496](https://doi.org/10.1093/mnras/stz3496)
- Milone, A. P., Piotto, G., Renzini, A., et al. 2017, *MNRAS*, 464, 3636, doi: [10.1093/mnras/stw2531](https://doi.org/10.1093/mnras/stw2531)
- Monty, S., Belokurov, V., Sanders, J. L., et al. 2024, *MNRAS*, 533, 2420, doi: [10.1093/mnras/stae1895](https://doi.org/10.1093/mnras/stae1895)
- Myeong, G. C., Evans, N. W., Belokurov, V., Sanders, J. L., & Koposov, S. E. 2018, *ApJL*, 863, L28, doi: [10.3847/2041-8213/aad7f7](https://doi.org/10.3847/2041-8213/aad7f7)
- Myeong, G. C., Vasiliev, E., Iorio, G., Evans, N. W., & Belokurov, V. 2019, *MNRAS*, 488, 1235, doi: [10.1093/mnras/stz1770](https://doi.org/10.1093/mnras/stz1770)
- Naidu, R. P., Ji, A. P., Conroy, C., et al. 2022, *ApJL*, 926, L36, doi: [10.3847/2041-8213/ac5589](https://doi.org/10.3847/2041-8213/ac5589)
- Navarro-Carrera, R., Caputi, K. I., Iani, E., et al. 2024, arXiv e-prints, arXiv:2407.14201, doi: [10.48550/arXiv.2407.14201](https://doi.org/10.48550/arXiv.2407.14201)
- Nissen, P. E., & Schuster, W. J. 2010, *A&A*, 511, L10, doi: [10.1051/0004-6361/200913877](https://doi.org/10.1051/0004-6361/200913877)
- Nomoto, K., Kobayashi, C., & Tominaga, N. 2013, *ARA&A*, 51, 457, doi: [10.1146/annurev-astro-082812-140956](https://doi.org/10.1146/annurev-astro-082812-140956)
- Pancino, E., Romano, D., Tang, B., et al. 2017, *A&A*, 601, A112, doi: [10.1051/0004-6361/201730474](https://doi.org/10.1051/0004-6361/201730474)
- Pilyugin, L. S., Vílchez, J. M., Mattsson, L., & Thuan, T. X. 2012, *MNRAS*, 421, 1624, doi: [10.1111/j.1365-2966.2012.20420.x](https://doi.org/10.1111/j.1365-2966.2012.20420.x)
- Plez, B. 2012, Turbospectrum: Code for spectral synthesis, Astrophysics Source Code Library, record ascl:1205.004
- Qiao, Y., Tang, B., Lian, J., Li, J., & Xu, C. 2024, *ApJ*, 961, 65, doi: [10.3847/1538-4357/ad0fd7](https://doi.org/10.3847/1538-4357/ad0fd7)
- Queiroz, A. B. A., Anders, F., Santiago, B. X., et al. 2018, *MNRAS*, 476, 2556, doi: [10.1093/mnras/sty330](https://doi.org/10.1093/mnras/sty330)
- Ramírez, I., Meléndez, J., & Chanamé, J. 2012, *ApJ*, 757, 164, doi: [10.1088/0004-637X/757/2/164](https://doi.org/10.1088/0004-637X/757/2/164)
- Reddy, B. E., Lambert, D. L., & Allende Prieto, C. 2006, *MNRAS*, 367, 1329, doi: [10.1111/j.1365-2966.2006.10148.x](https://doi.org/10.1111/j.1365-2966.2006.10148.x)
- Reddy, B. E., Tomkin, J., Lambert, D. L., & Allende Prieto, C. 2003, *MNRAS*, 340, 304, doi: [10.1046/j.1365-8711.2003.06305.x](https://doi.org/10.1046/j.1365-8711.2003.06305.x)
- Roederer, I. U., Preston, G. W., Thompson, I. B., et al. 2014, *AJ*, 147, 136, doi: [10.1088/0004-6256/147/6/136](https://doi.org/10.1088/0004-6256/147/6/136)
- Sanders, J. L., Belokurov, V., & Man, K. T. F. 2021, *MNRAS*, 506, 4321, doi: [10.1093/mnras/stab1951](https://doi.org/10.1093/mnras/stab1951)
- Savino, A., & Posti, L. 2019, *A&A*, 624, L9, doi: [10.1051/0004-6361/201935417](https://doi.org/10.1051/0004-6361/201935417)
- Sbordone, L., Bonifacio, P., Buonanno, R., et al. 2007, *A&A*, 465, 815, doi: [10.1051/0004-6361:20066385](https://doi.org/10.1051/0004-6361:20066385)
- Schiavon, R. P., Zamora, O., Carrera, R., et al. 2017, *MNRAS*, 465, 501, doi: [10.1093/mnras/stw2162](https://doi.org/10.1093/mnras/stw2162)
- Schönrich, R., Binney, J., & Dehnen, W. 2010, *MNRAS*, 403, 1829, doi: [10.1111/j.1365-2966.2010.16253.x](https://doi.org/10.1111/j.1365-2966.2010.16253.x)
- Senchyna, P., Plat, A., Stark, D. P., et al. 2024, *ApJ*, 966, 92, doi: [10.3847/1538-4357/ad235e](https://doi.org/10.3847/1538-4357/ad235e)
- Senchyna, P., Stark, D. P., Vidal-García, A., et al. 2017, *MNRAS*, 472, 2608, doi: [10.1093/mnras/stx2059](https://doi.org/10.1093/mnras/stx2059)
- Shetrone, M., Venn, K. A., Tolstoy, E., et al. 2003, *AJ*, 125, 684, doi: [10.1086/345966](https://doi.org/10.1086/345966)
- Shetrone, M., Tayar, J., Johnson, J. A., et al. 2019, *ApJ*, 872, 137, doi: [10.3847/1538-4357/aaff66](https://doi.org/10.3847/1538-4357/aaff66)
- Skúladóttir, Á., Tolstoy, E., Salvadori, S., Hill, V., & Pettini, M. 2017, *A&A*, 606, A71, doi: [10.1051/0004-6361/201731158](https://doi.org/10.1051/0004-6361/201731158)
- Snedden, C., Cowan, J. J., & Gallino, R. 2008, *ARA&A*, 46, 241, doi: [10.1146/annurev.astro.46.060407.145207](https://doi.org/10.1146/annurev.astro.46.060407.145207)
- Souza, S. O., Valentini, M., Chiappini, C., et al. 2024, *ApJL*, 977, L33, doi: [10.3847/2041-8213/ad91af](https://doi.org/10.3847/2041-8213/ad91af)
- Tang, B., Fernández-Trincado, J. G., Liu, C., et al. 2020, *ApJ*, 891, 28, doi: [10.3847/1538-4357/ab7233](https://doi.org/10.3847/1538-4357/ab7233)
- Tang, B., Liu, C., Fernández-Trincado, J. G., et al. 2019, *ApJ*, 871, 58, doi: [10.3847/1538-4357/aaf6b1](https://doi.org/10.3847/1538-4357/aaf6b1)
- Tang, B., Zhang, J., Yan, Z., et al. 2023, *A&A*, 669, A125, doi: [10.1051/0004-6361/202244052](https://doi.org/10.1051/0004-6361/202244052)
- Tang, B., Fernández-Trincado, J. G., Geisler, D., et al. 2018, *ApJ*, 855, 38, doi: [10.3847/1538-4357/aaaaea](https://doi.org/10.3847/1538-4357/aaaaea)
- Taylor, M. B. 2005, in Astronomical Society of the Pacific Conference Series, Vol. 347, Astronomical Data Analysis Software and Systems XIV, ed. P. Shopbell, M. Britton, & R. Ebert, 29

- Topping, M. W., Stark, D. P., Senchyna, P., et al. 2024, MNRAS, 529, 3301, doi: [10.1093/mnras/stae682](https://doi.org/10.1093/mnras/stae682)
- . 2025, ApJ, 980, 225, doi: [10.3847/1538-4357/ada95c](https://doi.org/10.3847/1538-4357/ada95c)
- Van der Walt, S., Colbert, S. C., & Varoquaux, G. 2011, Computing in Science and Engineering, 13, 22, doi: [10.1109/MCSE.2011.37](https://doi.org/10.1109/MCSE.2011.37)
- Virtanen, P., Gommers, R., Oliphant, T. E., et al. 2020, Nature Methods, 17, 261, doi: [10.1038/s41592-019-0686-2](https://doi.org/10.1038/s41592-019-0686-2)
- Vosegaard, T. 2018, Journal of Chemical Education, 95, 97, doi: [10.1021/acs.jchemed.7b00482](https://doi.org/10.1021/acs.jchemed.7b00482)
- Waskom, M. 2021, The Journal of Open Source Software, 6, 3021, doi: [10.21105/joss.03021](https://doi.org/10.21105/joss.03021)
- Weatherford, N. C., Kiroğlu, F., Fragione, G., et al. 2023, ApJ, 946, 104, doi: [10.3847/1538-4357/acbcc1](https://doi.org/10.3847/1538-4357/acbcc1)
- Wehrhahn, A. 2021, in The 20.5th Cambridge Workshop on Cool Stars, Stellar Systems, and the Sun (CS20.5), Cambridge Workshop on Cool Stars, Stellar Systems, and the Sun, 1, doi: [10.5281/zenodo.4537913](https://doi.org/10.5281/zenodo.4537913)
- Xu, C., Tang, B., Li, C., et al. 2024, A&A, 684, A205, doi: [10.1051/0004-6361/202347797](https://doi.org/10.1051/0004-6361/202347797)
- Yan, H., Li, H., Wang, S., et al. 2022, The Innovation, 3, 100224, doi: [10.1016/j.xinn.2022.100224](https://doi.org/10.1016/j.xinn.2022.100224)
- Yong, D., Norris, J. E., Bessell, M. S., et al. 2013, ApJ, 762, 26, doi: [10.1088/0004-637X/762/1/26](https://doi.org/10.1088/0004-637X/762/1/26)
- Yu, J., Tang, B., Fernández-Trincado, J. G., et al. 2021, ApJ, 913, 23, doi: [10.3847/1538-4357/abf64d](https://doi.org/10.3847/1538-4357/abf64d)
- Zhao, G., Zhao, Y.-H., Chu, Y.-Q., Jing, Y.-P., & Deng, L.-C. 2012, Research in Astronomy and Astrophysics, 12, 723, doi: [10.1088/1674-4527/12/7/002](https://doi.org/10.1088/1674-4527/12/7/002)

## APPENDIX

**Table A1.** The derived chemical abundances of 10 N-rich field stars with GALAH observations are listed here. The typical errors for all elements are also shown.

| Elements    | G1       | G2       | G3       | G4       | G5       | G6       | G7       | G8       | G9       | G10      | Error <sup>a</sup> |
|-------------|----------|----------|----------|----------|----------|----------|----------|----------|----------|----------|--------------------|
| RA (J2000)  | 289.4999 | 229.9611 | 330.4666 | 342.1356 | 91.8436  | 357.8821 | 330.2343 | 243.0392 | 73.4694  | 243.0330 | -                  |
| Dec (J2000) | -29.3267 | 2.3648   | -11.6966 | -23.8799 | -58.8617 | -3.2086  | -8.1948  | -24.6645 | -64.1526 | -25.0677 | -                  |
| [Fe/H]      | -1.202   | -0.723   | -1.420   | -1.159   | -0.806   | -0.708   | -0.912   | -1.075   | -0.842   | -1.250   | 0.05               |
| [C/Fe]      | -0.37    | -0.23    | -0.48    | 0.00     | 0.04     | 0.03     | 0.03     | 0.08     | 0.08     | -0.34    | 0.04               |
| [N/Fe]      | 0.86     | 0.53     | 0.93     | 0.61     | 0.54     | 0.62     | 0.80     | 0.87     | 0.54     | 0.86     | 0.04               |
| [O/Fe]      | 0.41     | 0.86     | 0.23     | 0.73     | 0.44     | 1.76     | 0.36     | 0.13     | 0.65     | 0.45     | 0.07               |
| [Na/Fe]     | 0.07     | -0.03    | 0.05     | 0.15     | 0.08     | 0.19     | 0.30     | 0.25     | -0.12    | 0.13     | 0.22               |
| [Al/Fe]     | 0.27     | 0.19     | 0.89     | 0.53     | 0.23     | 0.36     | 0.49     | 0.64     | 0.45     | 0.21     | 0.08               |
| [Mg/Fe]     | 0.38     | 0.29     | 0.15     | 0.48     | 0.62     | 0.20     | 0.27     | 0.20     | 0.63     | 0.28     | 0.05               |
| [Si/Fe]     | 0.14     | 0.19     | 0.17     | 0.52     | 0.28     | 0.17     | 0.21     | 0.29     | 0.40     | 0.08     | 0.02               |
| [Ca/Fe]     | -0.05    | 0.21     | 0.09     | 0.26     | 0.20     | 0.14     | 0.18     | 0.36     | 0.29     | 0.19     | 0.07               |
| [Ti/Fe]     | 0.10     | 0.01     | 0.13     | 0.35     | 0.35     | 0.18     | 0.25     | 0.30     | 0.45     | 0.20     | 0.04               |
| [Sc/Fe]     | 0.25     | -0.06    | 0.12     | 0.35     | 0.32     | 0.31     | 0.25     | 0.25     | 0.44     | 0.18     | 0.04               |
| [V/Fe]      | -0.08    | -0.14    | -0.15    | -0.01    | -0.08    | 0.08     | -0.07    | -0.12    | 0.13     | -0.18    | 0.06               |
| [Cr/Fe]     | 0.07     | -0.18    | -0.17    | -0.03    | -0.05    | -        | -0.08    | -0.12    | 0.10     | 0.21     | 0.04               |
| [Mn/Fe]     | -        | -        | -        | -0.35    | 0.13     | -0.40    | -0.41    | -0.52    | -0.06    | -        | 0.08               |
| [Co/Fe]     | 0.08     | 0.18     | 0.16     | 0.14     | 0.13     | 0.22     | 0.15     | 0.14     | 0.24     | 0.05     | 0.05               |
| [Ni/Fe]     | -0.11    | 0.05     | -0.20    | -0.15    | 0.09     | -0.09    | -0.09    | -0.10    | 0.07     | -0.23    | 0.04               |
| [Cu/Fe]     | -1.00    | -0.35    | -0.76    | -0.95    | -0.68    | -0.46    | -0.57    | -0.76    | -0.60    | -0.85    | 0.05               |
| [Zn/Fe]     | -        | -        | -        | -0.06    | -0.10    | -0.36    | -0.08    | -0.14    | -0.01    | -        | 0.03               |
| [Zr/Fe]     | -        | -        | -        | 0.13     | 0.28     | -0.22    | 0.14     | 0.23     | 0.61     | -        | 0.04               |
| [Ba/Fe]     | 0.09     | -0.03    | -0.18    | 0.59     | 2.01     | -0.07    | 0.23     | 0.23     | 2.00     | -0.10    | 0.05               |
| [La/Fe]     | -0.11    | -0.32    | 0.19     | 0.38     | 1.38     | -0.05    | -1.20    | 0.06     | 0.96     | 0.17     | 0.05               |
| [Ce/Fe]     | -        | -        | -        | 0.38     | 1.41     | 0.19     | 0.46     | 0.42     | 1.25     | -        | 0.04               |
| [Y/Fe]      | -        | -        | -0.52    | 0.46     | 1.10     | -0.36    | 0.30     | 0.08     | 0.91     | -0.02    | 0.05               |
| [Eu/Fe]     | 0.20     | 0.29     | 0.53     | 0.32     | 0.76     | 0.48     | 0.35     | 0.34     | 0.77     | 0.25     | 0.06               |
| [Nd/Fe]     | 0.23     | 0.41     | 0.77     | 0.78     | 1.39     | 0.42     | 0.64     | 0.57     | 1.21     | 0.48     | 0.04               |

NOTE—<sup>a</sup>: Typical abundance error of each element.

**Table A2.** Observation information of 33 N-rich field stars studied in this work.

| Object Name | Gaia Source ID      | Source   | S/N<br>(around 6000 Å) | Observation Date |
|-------------|---------------------|----------|------------------------|------------------|
| Num28       | 364641868732115584  | CFHT     | 121                    | 2020-11-30       |
| Num32       | 701587619382431488  | CFHT     | 84                     | 2020-12-04       |
| Num24       | 3165682645690499840 | CFHT     | 82                     | 2020-12-05       |
| Num7        | 646620280034177664  | CFHT     | 77                     | 2020-12-05       |
| Num63       | 1323227854226937984 | CFHT     | 81                     | 2021-08-28       |
| Num1        | 1366614235165728000 | CFHT     | 96                     | 2021-08-28       |
| Num37       | 3602560813461369984 | CFHT     | 71                     | 2023-06-27       |
| Num10       | 2100388163371964928 | CFHT     | 61                     | 2023-07-10       |
| Num9        | 3277155365059485696 | Magellan | 115                    | 2020-02-26       |
| Num38       | 4395247566817046400 | Magellan | 171                    | 2020-02-27       |
| Num47       | 3646613262223485184 | Magellan | 160                    | 2020-02-28       |
| Num58       | 3628603811516372864 | Magellan | 93                     | 2020-02-28       |
| Num62       | 3090695166699934080 | Magellan | 130                    | 2020-02-27       |
| Num65       | 4417483269639370880 | Magellan | 152                    | 2020-02-27       |
| Num67       | 2685646524818105344 | Magellan | 56                     | 2019-07-24       |
| Num69       | 3835184248030417664 | Magellan | 149                    | 2020-02-28       |
| Num80       | 576599363783579008  | Magellan | 129                    | 2020-02-27       |
| Num82       | 3628877246314114176 | Magellan | 175                    | 2020-02-28       |
| Num86       | 4455038291879056384 | Magellan | 51                     | 2019-07-24       |
| Num88       | 4452741961844020992 | Magellan | 54                     | 2019-07-24       |
| Num94       | 3866576748112550400 | Magellan | 62                     | 2020-02-28       |
| Num97       | 1174906033445812352 | Magellan | 57                     | 2019-07-24       |
| Num98       | 3733311094103785344 | Magellan | 184                    | 2020-02-28       |
| G1          | 6759421390173629952 | GALAH    | 80                     | 2017-07-25       |
| G2          | 4421607950076317184 | GALAH    | 88                     | 2023-05-04       |
| G3          | 2613662391901002240 | GALAH    | 87                     | 2017-06-02       |
| G4          | 6623590781687449856 | GALAH    | 108                    | 2017-09-12       |
| G5          | 5494723292962635904 | GALAH    | 138                    | 2017-12-06       |
| G6          | 2447417402012872960 | GALAH    | 172                    | 2016-11-06       |
| G7          | 2618486563591431680 | GALAH    | 126                    | 2014-07-12       |
| G8          | 6049790293472210560 | GALAH    | 184                    | 2014-07-08       |
| G9          | 4664662314020413952 | GALAH    | 118                    | 2016-10-14       |
| G10         | 6049561049599634304 | GALAH    | 77                     | 2014-07-13       |

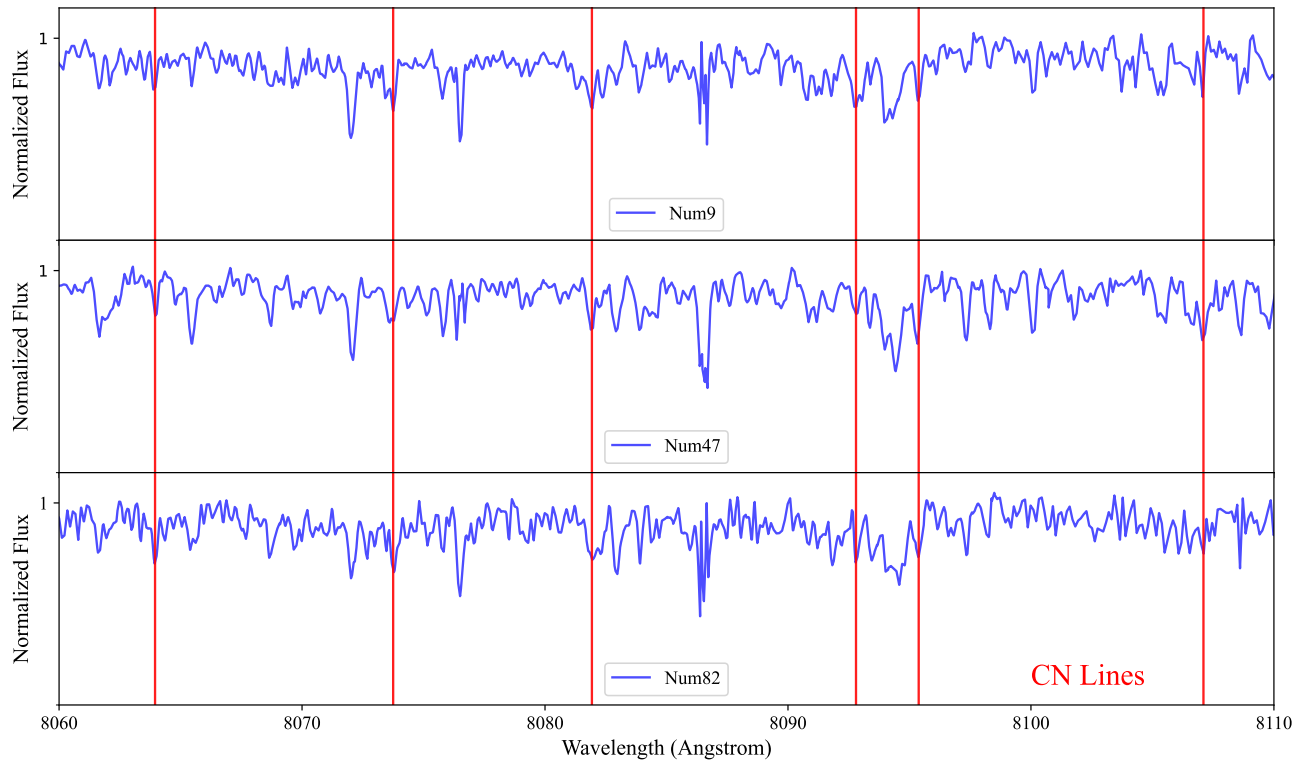


**Figure A1.** Sample spectra for 3 N-rich field stars studied in this work. Num47 and Num82 have converged C/N abundances and Num9 does not. The central wavelengths of feature CN lines are marked with red solid lines.